Journal of
Composites Science

MDPI

Article

Preliminary Experimental and Numerical Study of Metal Element with Notches Reinforced by Composite Materials

Paweł J. Romanowicz [1,*], Bogdan Szybiński [1] and Mateusz Wygoda [2]

[1] Faculty of Mechanical Engineering, Cracow University of Technology, ul. Warszawska 24, 31-155 Cracow, Poland; bogdan.szybinski@pk.edu.pl
[2] Department of Product Technology and Ecology, College of Management and Quality Sciences, Cracow University of Economics, 31-510 Cracow, Poland; mateusz.wygoda@uek.krakow.pl
* Correspondence: pawel.romanowicz@pk.edu.pl

Abstract: The presented study is related to the application of the composite overlays used in order to decrease the effect of the stress concentrations around the cut-outs in structural metal elements. The proposed approach with the application of the digital image correlation extends the recently presented studies. Such structural elements with openings of various shapes have been accommodated for a wide range of industrial applications. These structures exhibit certain stress concentrations which decrease their durability and strength. To restore their strength, various reinforcing overlays can be used. In the present paper, the flat panel structure without and with the composite overlays made of HEXCEL TVR 380 M12/26%/R-glass/epoxy is under the experimental and the numerical study. Particular attention is paid to the investigation of the samples with the rectangular holes, which for smooth rounded corners offer a higher durability than the samples with the circular hole of the same size. The experimental results are obtained for the bare element and are reinforced with composite overlay samples. The experimental results are obtained with the use of the Digital Image Correlation method, while the numerical results are the product of the Finite Element Analysis. In the numerical analysis, the study of the shape, size and fiber orientation in applied overlays is done. The reduction of the stress concentration observed in opening notches has confirmed the effectiveness of the overlay application. In the investigated example, the application of the square composite overlay increased the structure strength even by 25%.

Keywords: holes; composites; reinforcements; digital image correlation; tensile tests

Citation: Romanowicz, P.J.; Szybiński, B.; Wygoda, M. Preliminary Experimental and Numerical Study of Metal Element with Notches Reinforced by Composite Materials. *J. Compos. Sci.* **2021**, *5*, 134. https://doi.org/10.3390/jcs5050134

Academic Editor: Konda Gokuldoss Prashanth

Received: 27 April 2021
Accepted: 11 May 2021
Published: 18 May 2021

1. Introduction

The structural elements with voids or openings of different shapes are commonly used in design practice. The main reason for this is that it is necessity to provide access to certain parts of the structure or the possibility to supply power or other media to perform the production process or correct operation. Such intentionally made holes are usually the source of the stress concentration, which may substantially decrease the structure durability or the fatigue endurance in cases of repetitive loading imposition. Another possible danger is the appearance of zones with plastic deformations, which are usually not allowed in standard structure operations. Such zones around the different holes have been recently analyzed using the Digital Image Correlation (DIC) [1], which is under rapid development and is successfully used for damage monitoring of different materials, such as isotropic metals [1], cementitious composites [2], and composites [3]. In the presented paper, special attention is focused on the reduction of such stress concentrations in notches reached through the application of the composite overlays around the cut-out hole.

The problem of stress concentration in constructional elements has attracted researchers for more than one hundred years and is still under thorough study due to the application of more and more advanced materials and the increasing shape complexity of the structural elements [1,3–25]. The first, basic mathematical formulas for the plane

isotropic panels with openings were published by Kirsch [5], Kolosov [6] and Inglis [7]. In the next few years further development concerned both the search of analytical solutions for more complex shapes of stress raisers [8–11] and non-isotropic materials [12]. The general drawback of these early solutions relied on modeling mainly infinite elements, which are not applicable to the real designing practice. For this purpose, certain papers, including the respective corrective procedures for finite-size elements, were published over the years [3,13–16]. The pure mathematical considerations were supplemented by the intensive development of experimental studies verifying the theoretical results [17–19]. The results of these studies are gathered in various designer's guides, standards and codes of practice used in design [20–25]. Nowadays, these manuals serve mainly for the control of solutions obtained by means of numerical methods. Among them, the Finite Element Method [26] is of great importance and enables the calculation and real assessment of the stress concentration factors for very complex shapes and general loads.

In order to attenuate the adverse impact of the stress raiser's presence, various approaches have been proposed. If we consider the typical structure with various holes or cross-bores like standard pressure vessels located in the distance outlet and inlet stub pipes and inspection hatches, the most obvious and simplest one is the simple load or pressure reduction, but this results in the underload of certain parts of the vessel, for which thickness is in the first step set using formulas for solid continuous panels or tubes [27]. The most common and popular method of cross-bore reinforcement is the application of the overlays in the cut hole area, welded around the stub and over the boiler shell, which releases the stress concentration taking over part of the load. This method is particularly suitable for vessels with distant stubs and hatches, and provides material savings. The latter approach has also been adopted for other structures like beams, spans of bridges [28,29] and other constructional elements not only for reinforcement but also for restoring the load capacity in elements with cracks and microvoids. In such solutions not only the same materials are used. In recent years the connection of different materials has become more and more popular due to the development, in particular, of composite materials and bonding techniques. The number of such solutions has increased drastically in many industries, particularly in the automotive or aviation industry and others and is reflected by the growing year-to-year number of papers [30–41].

The connection technique generally depends on the application and material behavior [42]. The most commonly used are adhesive joints (i.e., automobile industry) and adhesive with mechanical fasteners (i.e., aircrafts). The types and advantages of the adhesive connections are described in Refs. [43–45]. The main failure forms of the adhesive joints are adhesive failure, cohesive failure, thin-layer cohesive failure, stock-break failure, fiber-tear and light-fiber-tear failure and adherend failure outside the joint [38,44,45]. The significant influence on the joint strength has a suitable selection of the adhesive material. Such effects for the AW-7075 aluminum alloy with aramid-epoxy and carbon-epoxy composite joints were studied by Rudawska [37], Wang Z.Y. with coworkers [30,31] or Aljabar [33]. It was observed that the increase in the joint strength can be achieved by the application of more flexible adhesive.

The important problem concerning metal-composite bonded connections is the analysis of shear stresses in the adhesive joints. Such problems can be solved with the use of the finite element method. There are also available limited theoretical solutions for typical adhesively bonded joints. From the historical point of view, the two models proposed by Volkersen [46] and Goland and Reissner [47] should be cited. The first theoretical solution (called Volkersen's single-lap theory) was proposed by Volkersen in 1938 [46] in which the concept of the differential shear is introduced. In this concept, it is assumed that only an elastic tensile strain occurs in the adherents and only shear effect occurs in the adhesive. Goland and Reissner [47] proposed the formulation in which the bending moment in the adhesive joint is also included. Based on the above theories, different 2D and 3D models are proposed. Interesting from the point of view of this work is the theoretical solution for single-bonded stiffened joints proposed by Ghoddous [41]. The results obtained for

a single stiffened joint (from theoretical and numerical calculations) signalize significant stress concentrations at the ends of the adhesive joints. More information about such theoretical formulations can be found in Refs. [41,44,45]. There are also methods for analyzing materials at the macro-, meso-, and micro-levels [48,49]. Despite the many theoretical models as well as techniques (fracture mechanics [38,50], cohesive zone model [40,45], FEM [39,45,51,52], continuum mechanics), there is no universal approach for predicting the strength of adhesive joints [44].

Based on the Volkersen solution [46], the shear stress in the adhesive layer varies along the overlap length. Such shear stresses depend on the strain distribution in the adherents. Due to the differences in deformations, the highest shear stresses in the adhesive occur at both ends and are minimal at the center of the adhesive joint. It should be noted that stress concentrations of the shear stresses in the adhesive layer may achieve high values (typically 1–4, but in some cases even above 10) [40,41,45,51]. Because of this, the failure typically initiates at both ends of the adhesive joint [40,52]. Due to the high-stress concentrations at the ends of the adhesive joint and degradation of the adhesive layer over time, such connections require periodic inspections in order to control and repair damages. Such monitoring can be made with the use of the traditional non-destructive techniques [45,53], vibration-based methods [35], digital image correlation [1,3] or c-scan inspection [54].

Except for the problems with the adhesive joint choice, several advantages are present in a metal adhesive layer composite material combination. These are attributed to the nature of the composite material. The number of composite layers, choice of fiber material and matrix resin type, orientation of fibers in stacking layers and the size of the overlay can be freely shaped during the study of the overlays, and the above parameters can be the subject of the optimal choice for the analyzed problem.

The main aim of the presented paper is the experimental and numerical study of possibilities of reduction of the effect of the stress concentrations on the structure strength under tensile load. The proposed approach, with the application of the digital image correlation, extends the recently presented studies. The analyses are performed for metal samples with rectangular holes reinforced by the composite overlays. The reduction of the stress concentration observed in opening notches has confirmed the usefulness of the overlay application. In the investigated example, the application of the square composite overlay increased the structure strength even by 25%. The paper consists of five sections. The introduction to the studied problem and the literature review is given in Section 1. The description of the applied materials, samples and methods are described in Section 2. The results of the experimental investigations are presented and discussed in Section 3. The results of the numerical analyses are presented in Section 4. In these numerical studies, the influence of the geometry of the overlays and orientations of the layers on the structural strength is examined. The summary of the performed study and the final discussion are given in Section 5. The conclusions are given in Section 6.

2. Materials and Methods

Materials and Samples

The presented numerical and experimental studies are made for the samples made of structural steel with different cut-outs reinforced by composite overlays. The structural low-alloy steel S355J2+N was used as the base material. Such steel can be characterized by high strength and ductility, as well as good weldability, and is generally used in the manufacturing of machine parts, pressure vessels and pipes, and in civil engineering. The chemical composition of the material used in the experimental tests is given in Table 1. The maximal values of the particular chemical elements, as well as the minimal mechanical properties according to Standards [55], are also reported in Table 1.

Table 1. Chemical composition and mechanical properties of S355J2+N steel.

Chemical Components of S355J2 Steel (in Weight %)									
Material	**C**	**Si**	**Mn**	**P**	**S**	**Cu**	**Al**	**Cr**	**Fe**
S355J2+N (tested material)	0.19	0.20	0.99	0.012	0.01	0.03	0.04	0.02	res.
S355J2, Standards [55], max %	0.20–0.22	0.55	1.60	0.025	0.025	0.55	-	-	res.
Mechanical Properties of S355J2 Steel									
Material (EN)	**Material (AISI, ASTM)**	**Upper Yield Limit Y_{eH}**				**Tensile Strength R_m**			
S355J2 [55]	A765	Min. 355 MPa				470–630 MPa			

The reinforcement overlays were made of TVR 380 M12/26%/R-glass/epoxy composite material. The plate used in the preparation of the reinforcement overlays was made from prepregs with fiber and epoxy resin densities equal to 2.56 g·cm^{-3} and 1.24 g·cm^{-3}, respectively. More details about the preparation of the composite plate, including information about the autoclave operation, can be found in Ref. [56]. The mechanical properties of the composite material were determined with the use of the experimental tests for samples with orientations $\theta = [0°]_8$, $\theta = [90°]_8$, $\theta = [+45°/-45°]_4$ ($\theta = 0°$ is the direction of the tension) according to the Standards [57]. Four samples were tested for each of the above cases with the loading rate equal to 3 mm/min. The detailed description and results of the tensile tests are presented in Ref [56], and the most important information is reported in Table 2. The obtained mechanical properties of composite material are in good agreement with the literature data [58].

Table 2. Mechanical properties of composite material.

Material	**E_1 [GPa]**	**E_2, E_3 [GPa]**	**G_{12}, G_{13} [GPa]**	**G_{23} [GPa]**	**ν_{12},ν_{13}**	**ν_{23}**	**Tensile Strength (MPa)**		
							$[0°]_8$	**$[90°]_8$**	**$[+45°/-45°]_4$**
HEXCEL TVR 380 M12/26%/R-glass/epoxy	46.43	14.92	5.23	9.15	0.269	0.3	1601 SD [1]:59.2	68.7 SD:6.7	141.8 SD:8.4

[1] Standard deviation (in MPa).

The behavior of the composite samples is presented in the form of the stress–strain curves in Figure 1. The failure form depends on the orientation of the fiber to the tensile loading. In the first case (Figure 1a—$\theta = [0°]_8$) rapid fracture with fiber cracking occurred. In the second case (Figure 1b—$\theta = [+45°/-45°]_4$) slow matrix cracking and separation of the fibers from the matrix were observed in the whole volume of the sample. In the last case (Figure 1c—$\theta = [90°]_8$) rapid matrix cracking occurred. For this configuration, greater variance of the tensile strength is achieved. This may be caused by the geometry of the sample or matrix strength. However, the mean value from the tensile test is in good agreement with the literature data [58]. The average tensile strengths for investigated orientations are reported in Table 2.

The stress–strain curve of the base S355J2+N material was determined with the use of the sample with geometry given in Figure 2a. The dimensions of the sample were set according to the Standards [59]. The main experimental tests were carried for the samples with circular Ø15 mm (Figure 2b) and rectangular 15 × 15 mm holes. In the case of rectangular cut-outs, two fillet radii were assumed—R2 (Figure 2c) and R4 (Figure 2d). The hole was located at the center of the plate. The thickness of the base metal samples was 4 mm. The final test was made for the sample with reinforcement overlays on both sides (Figure 2e). The loading rate of tensile tests was equal 0.5 mm/min. More information about tests and samples are summarized in Table 3.

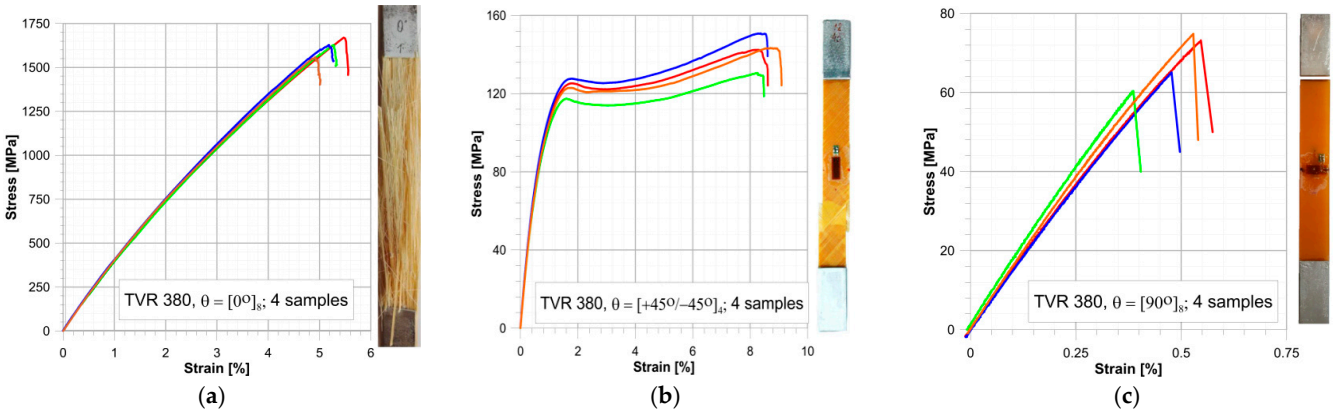

Figure 1. Stress–strain curves for samples made of TVR 380 with stacking sequence: (**a**) $\theta = [0^\circ]_8$; (**b**) $\theta = [+45^\circ/-45^\circ]_4$; (**c**) $\theta = [90^\circ]$.

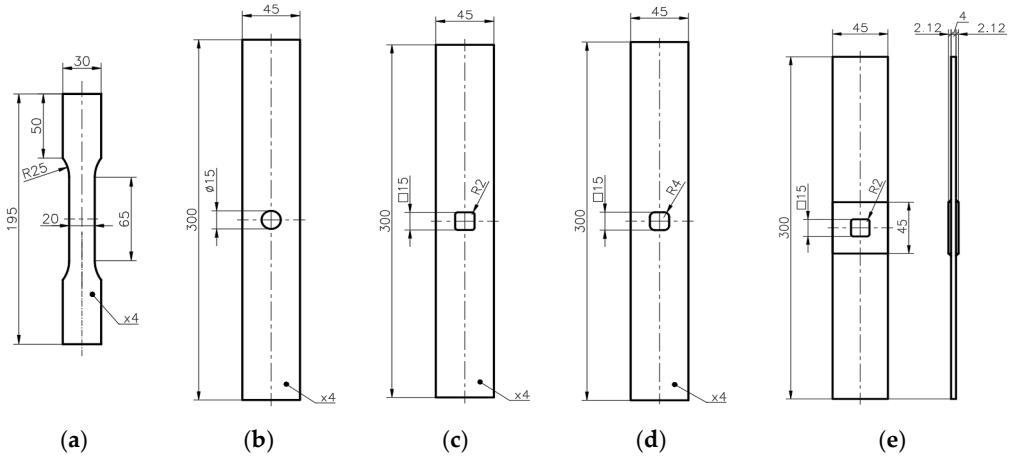

Figure 2. Geometry and dimension of tested samples made of: (**a**) S355J2+N; (**b**) S355J2+N with circular hole; (**c**) S355J2+N with rectangular hole with fillet radius R2; (**d**) S355J2+N with rectangular hole with fillet radius R4; (**e**) S355J2+N with rectangular hole with fillet radius R2 with reinforcement overlays made of TVR 380 with layer orientation $[+45^\circ/-45^\circ]_4$.

Table 3. Description of investigated samples.

No. of Sample	Geometry	Hole Type	Material	Remarks
1	Figure 2a	-	S355J2+N	-
2	Figure 2b	Circular ϕ15 mm	S355J2+N	-
3	Figure 2c	square 15 × 15 mm	S355J2+N	corner fillet radii 2 mm
4	Figure 2d	square 15 × 15 mm	S355J2+N	corner fillet radii 4 mm
5	Figure 2e	square 15 × 15 mm	S355J2+N/TVR 380 $\theta = [+45^\circ/-45^\circ]_4$	corner fillet radii 2 mm

The overlays with a rectangular shape and dimensions 45 × 45 mm were made of the TVR 380 glass/epoxy composite material with the layer orientation $\theta = [+45^\circ/-45^\circ]_4$ (Figure 3). The thicknesses of the overlays were equal to about 2.12 mm. The microscopic image of the composite overlay through its thickness is also given in Figure 3c. The overlays were stuck to the metal base part with the use of S&P Resin 220 epoxy adhesive, which is dedicated to the reinforcement of steel structures by fiber composites. The compressive and shear strength of the used resin should not be less than 70 MPa and 26 MPa, respectively, and the minimum modulus of elasticity is equal to 7100 MPa. The epoxy adhesive was applied between the surfaces of the reinforcement overlays and the base metal part (red

color in Figure 3a) and at both ends of composite overlays. The angle of the epoxy adhesive triangular spew fillets at the ends of the overlays was 45° for load transfer over a larger area.

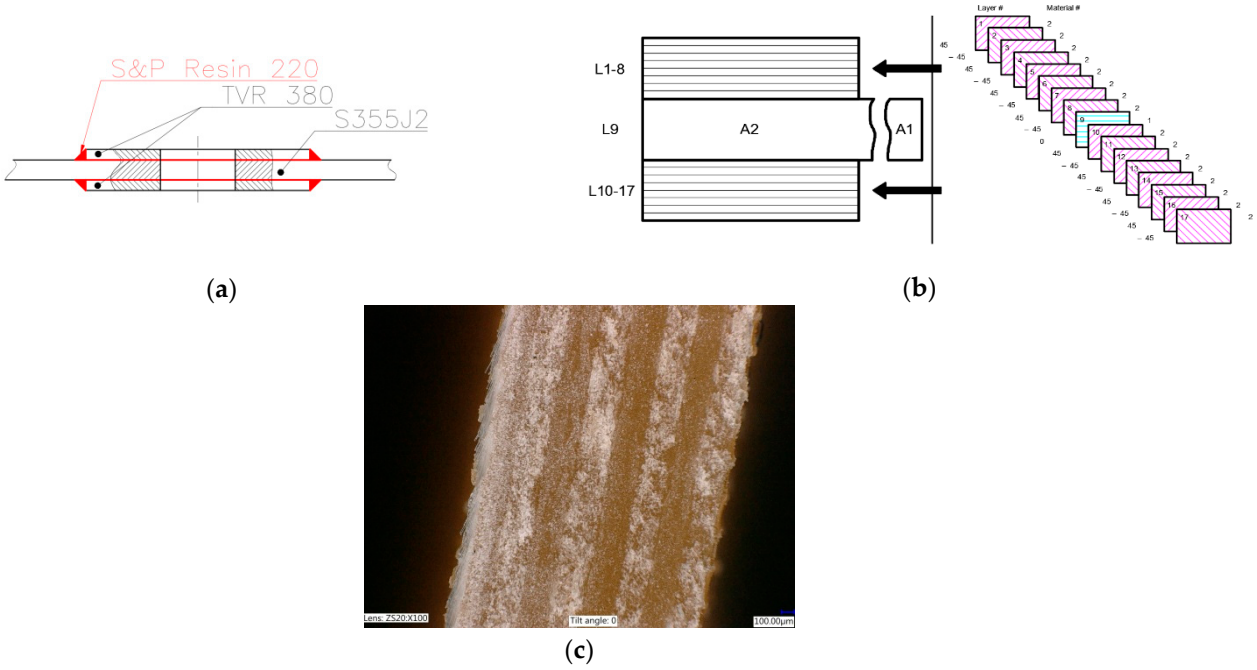

Figure 3. Design of sample 5 with composite overlays: (**a**) structure of adhesive joint; (**b**) stacking sequence and numbering of layers; (**c**) microscopic image of the composite $[+45^\circ/-45^\circ]_4$ material.

The prepared samples with holes made of S355J2+N are presented in Figure 4 and the sample with composite reinforcement overlays is presented in Figure 5. The surfaces of the samples were covered with random black speckle patterns with various shapes on a white background. This black/white coating with randomly distributed speckle patterns was necessary for the application of the digital image correlations (DIC). This technique allows determining the distribution of the strain field on the tested surface. For this purpose, a series of photographs with constant time intervals (with the use of the Nikon D90 camera) were made during the tensile tests. The DIC analyses were made in the GOM Software [60]. The photographs were made in the constant time interval equal to 6 seconds. All analyses performed in GOM were made with the same configuration—the facet size and the point distance were equal to 66 and 15 pixels, respectively.

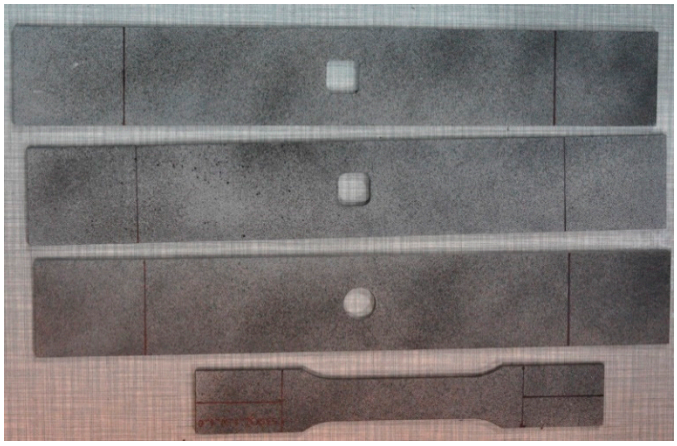

Figure 4. Photograph of tested samples 1–4 covered by speckle patterns.

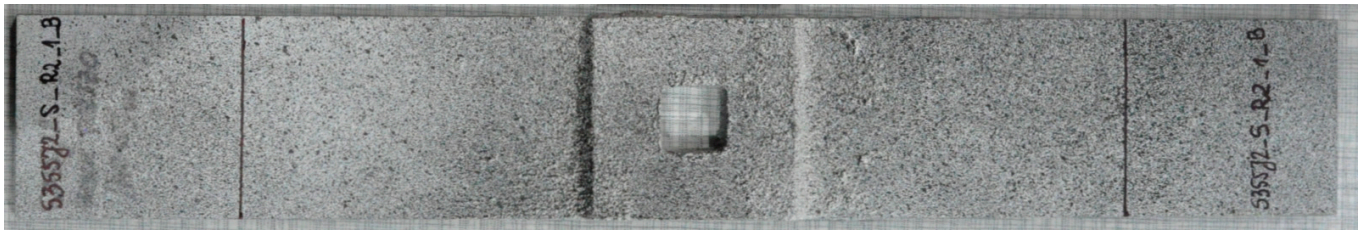

Figure 5. Photograph of sample 5 with composite reinforcement overlays at the center and covered by speckle pattern.

3. Experimental Tests

3.1. Stress–Strain Behavior of S355J2+N

The engineering stress–strain curve for S355J2+N (Figure 6) was designated with the use of the sample presented in Figure 2a. The determined upper Yield limit was higher than its minimum value [55] and was equal to 372 MPa (point 1 in Figure 6). After reaching the upper Yield limit, a slight reduction of the stress was observed. The S355J2+N material showed the Yield plateau (the range between points 1 and 2 in Figure 6) before strengthening. The maximal registered stress was equal to 543 MPa (p.3 in Figure 6). The elongation of the sample after fracture was equal to ε_{TOT} = 31.5%.

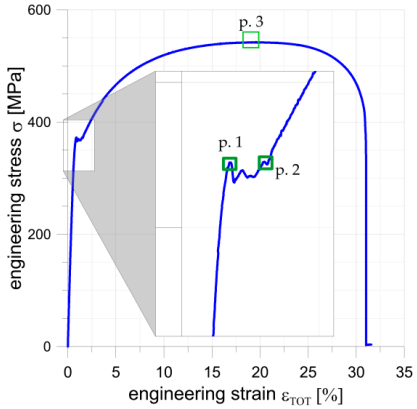

Figure 6. Engineering stress–strain curve obtained for sample 1 made of S355J2+N.

The development of the strain field on the surface was studied with the use of DIC. Such analyses were carried in the range of strain from strain, corresponding to the upper Yield limit (ε_{TOT} = 0.85%—Figure 7a) to the material strengthening (ε_{TOT} = 3.39%—Figure 7f). Uniform stretching of the sample was observed up to the Yield limit (Figure 7a). Above the Yield limit (point 1 in Figure 6), the strong concentration of the strain appeared in the weakest point and cross-section of the sample (Figure 7b). In the range of the Yield plateau (Figure 7b–d), the growth of the plastic strain in the surrounding of the weakest cross-section was observed. For the strain ε_{TOT} = 1.40% the second strain concentration appeared (Figure 7d). A further increase of tension leads to the plasticizing of the whole test part of the sample (Figure 7e) and strengthening (Figure 7f). The determined stress–strain curve was used for material description in the FE simulations. The failure form is presented in Figure 8.

3.2. Unreinforced Metal Samples with Holes

The influence of the stress concentrators in a form of circular and rectangular cut-outs in metal plates was investigated by the Authors in Ref. [1] Such holes or notches may significantly reduce the structure strength. Generally, the value of the stress concentration factor, denoted as K_t, can be described by the given below formula:

$$K_t = K_t^{INF} C_W = \left[C_0 + C_1(f_1) + C_2(f_2)^2 + C_3(f_3)^3\right] C_W, \quad (1)$$

where: K_t^{INF} is the stress concentration factor for infinity plate, C_W is the correction constant for a plate with finite width, C_0, C_1, C_2, C_3 are the constant dependent on the cut-out shape, and f_1, f_2, f_3 are the functions dependent on the characteristic dimensions of the cut-out.

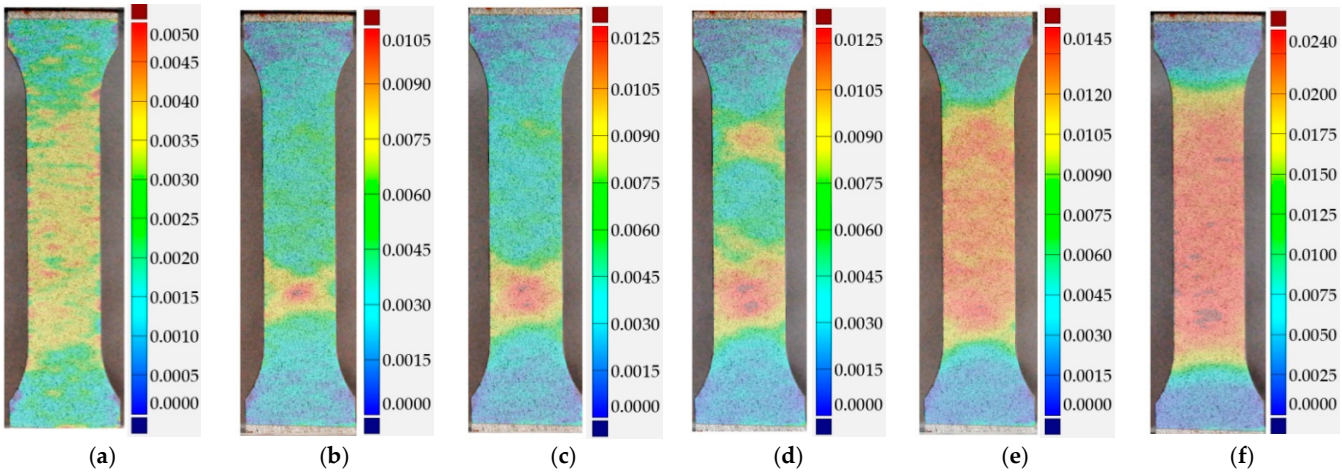

Figure 7. Distribution of strain on the surface for sample 1 for strain: (**a**) ε_{TOT} = 0.85%; (**b**) ε_{TOT} = 1.12%; (**c**) ε_{TOT} = 1.27%; (**d**) ε_{TOT} = 1.40%; (**e**) ε_{TOT} = 1.97%; (**f**) ε_{TOT} = 3.39%.

Figure 8. Photograph of sample no.1 after failure.

The detailed formulae concerning the stress concentration factors for both rectangular and circular holes can be found in Refs. [1,21–24]. The calculated theoretical values of the above constants, as well as stress concentration factors, are summarized in Table 4. Obviously, the largest value of K_t = 2.479 was obtained for the sample with the rectangular hole with the smallest fillet radius R2. However, based on the theoretical calculations, it is interesting that the circular hole is not the optimal one. It can be seen that the rectangular hole with a sufficiently large fillet radius shows smaller concentrations of stresses than the circular hole. Due to this fact, in the presented preliminary studies of the reinforcing of the metal plates with cut-outs with the use of composite overlays, the experimental studies were performed for sample 3 with the largest K_t.

Table 4. Theoretical values of stress concentration factors for investigated samples.

Cut-out	K_t	C_0	C_1	C_2	C_3	f_1	f_2	f_3	K_t^{INF}	C_W	Remarks
Circular (sample 2)	2.314	2.000	0.284	−0.600	1.320	$1 - d/W = 0.667$	$1 - d/W$	$1 - d/W$	2.314	1	D = 15 mm W = 45 mm
Rectangular R2 [1] (sample 3)	2.479	8.842	−13.676	12.847	−4.518	$b/a = 1$	b/a	b/a	3.495	0.709	$R/b = 2/15$ $b/W = 1/3$
Rectangular R4 [1] (sample 4)	2.084	7.641	−13.202	13.808	−5.309	$b/a = 1$	b/a	b/a	2.939	0.709	$R/b = 4/15$ $b/W = 1/3$

[1] Values in rows are valid only for the same ratios R/b and b/W.

The stress–strain characteristics for samples 2–4 with circular and rectangular holes are given in Figure 9. In the elastic and strain strengthening range till to strain ε_{TOT} = 1.5%, all three samples show similar characteristics. A slightly greater force in this range

(ε_{TOT} = 0–1.5%) was registered for the sample with the circular hole. However, the maximal tensile forces (the ultimate tensile strength) were slightly greater in both samples with rectangular holes. The most significant difference in the behavior of these samples was the maximal elongation, which in the case of the sample with the circular hole was almost two times smaller than for samples with rectangular holes.

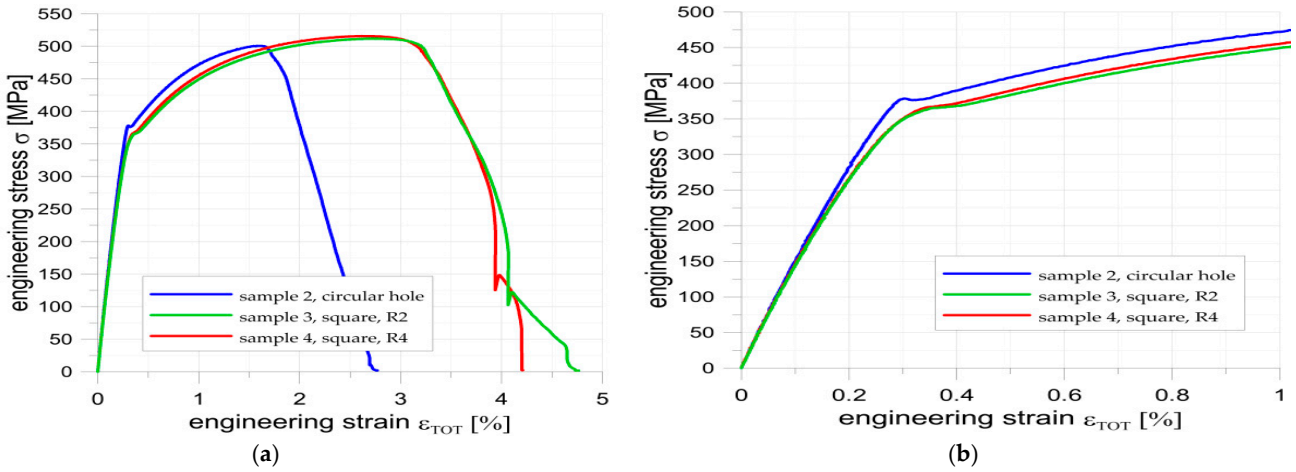

Figure 9. Engineering stress–strain curve for samples 2–4 made of S355J2+N with cut-outs: (**a**) behavior in full range of strain; (**b**) enlargement of initial range of strain.

The development of plastic strains on the surfaces of the tested samples, designated with the use of DIC, are presented in: Figure 10 for the sample with the circular hole; Figure 11 for the sample with the rectangular hole with fillet radius R2 and Figure 12 for the sample with the rectangular hole with fillet radius R4. In all the presented examples, the failure occurred in the weakest cross-section (Figure 13). In the case of the sample with the circular hole, the crack direction was horizontal and was initiated in two points at which the highest strain concentrations were determined in DIC analysis (Figure 10). In the case of the rectangular hole with rounded corners, the cracks were initiated in points on the vertical edge of the hole below the fillet radius. In both cases, such cracks appeared on the opposite corners of the rectangular hole. It can be seen that in the points at which cracks are initiated (Figure 13), high stress (strain) concentrations are registered (Figures 11 and 12).

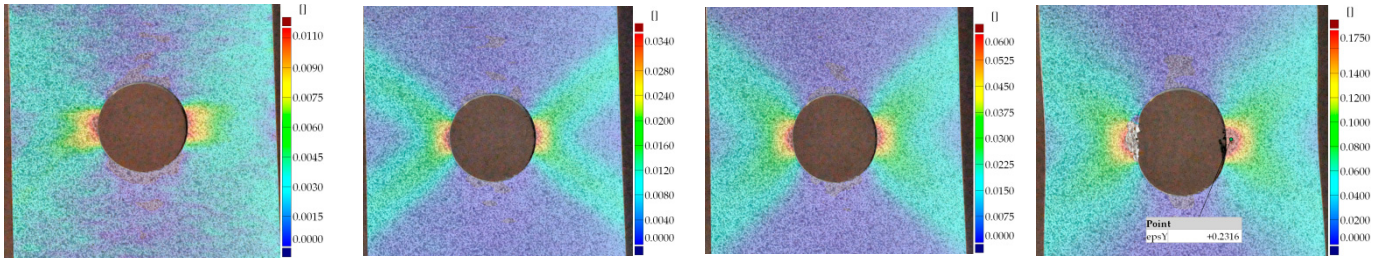

Figure 10. Distribution of strains on the surface for sample no. 2 with circular holes for strain: (**a**) ε_{TOT} = 0.45%; (**b**) ε_{TOT} = 0.50%; (**c**) ε_{TOT} = 0.75%; (**d**) ε_{TOT} = 1.58.

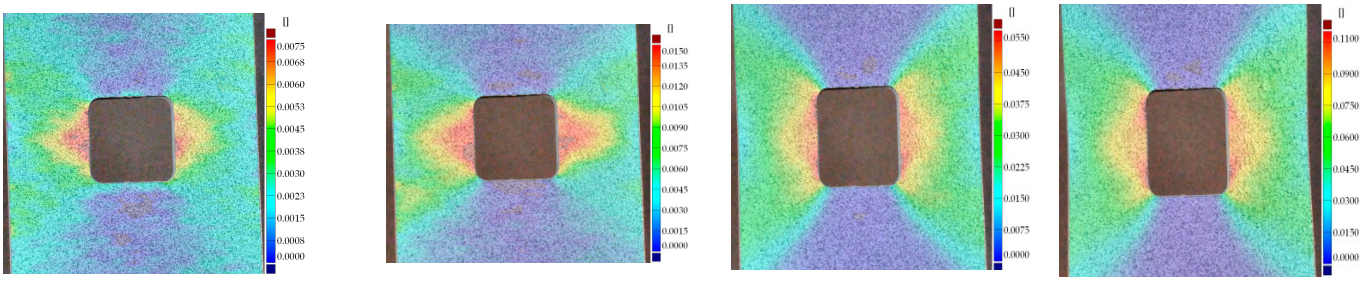

(a) (b) (c) (d)

Figure 11. Distribution of strains on the surface for sample no. 3 with rectangular holes with a fillet radius R2 for strain: (**a**) ε_{TOT} = 0.3%; (**b**) ε_{TOT} = 0.37%; (**c**) ε_{TOT} = 0.85%; (**d**) ε_{TOT} = 1.48%.

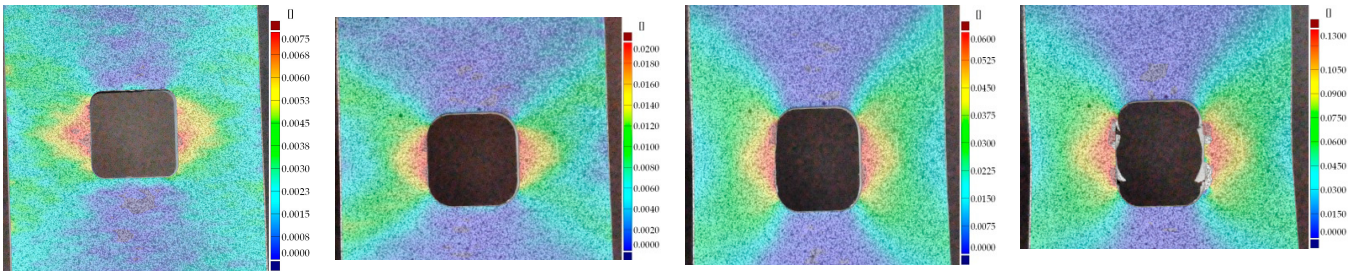

(a) (b) (c) (d)

Figure 12. Distribution of strains on the surface for sample no. 4 with rectangular holes with a fillet radius R4 for strain: (**a**) ε_{TOT} = 0.35%; (**b**) ε_{TOT} = 0.40%; (**c**) ε_{TOT} = 0.85%; (**d**) ε_{TOT} = 1.63%.

(a) (b) (c)

Figure 13. Failure forms of tested samples: (**a**) sample no.2 with a circular hole; (**b**) sample no. 3 with a rectangular hole with a fillet radius R2; (**c**) sample no. 4 with a rectangular hole with a fillet radius R4.

3.3. Metal Samples with Holes Reinforced by Composite Materials

The main aim of the study was the analysis of the behavior of the composite reinforcement of the metal part with cut-out. The preliminary experimental test was performed for the sample with the rectangular hole with a fillet radius R2. The selection of the cut-out shape was based on the results of the experimental tests described in Section 3.2. The selected sample revealed the highest stress concentration factor with maintaining a high load capacity at the upper Yield limit of the material and ultimate tensile strength and high elongation at the fracture. The determined stress–strain curve for the metal with composite overlays (sample 5) is given in Figure 14. The stress in Figure 14 was calculated as a nominal stress in a metal plate with a cut-out with the given below formula:

$$\sigma = \frac{F}{(W-a)t}, \quad (2)$$

where: F is the measured force, W and t are the width and the thickness of the metal plate, respectively, and a is the width of the hole.

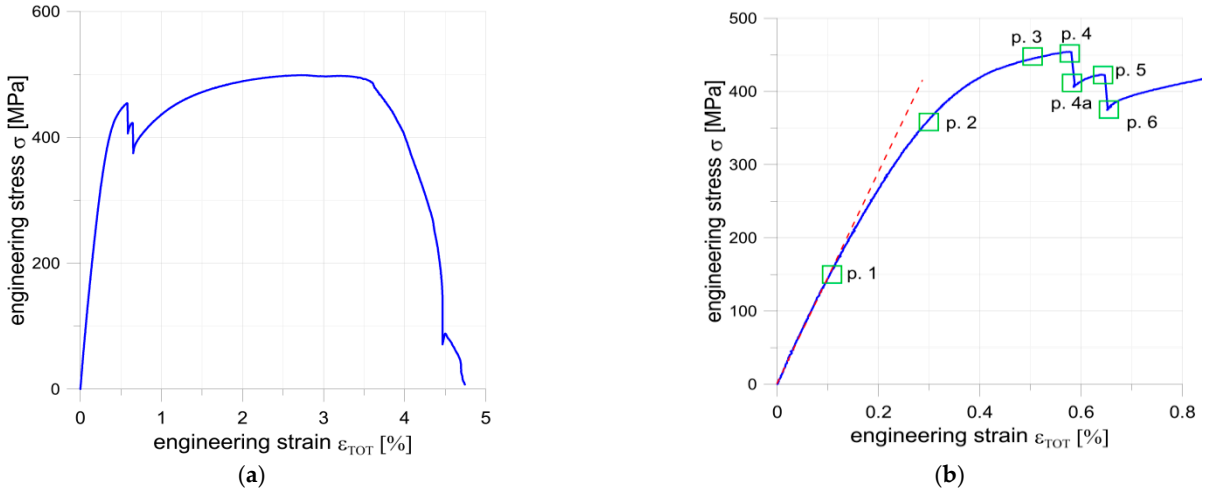

Figure 14. Engineering stress–strain curve for sample no. 5 with a rectangular cut-out with a fillet radius R2 and composite overlays: (**a**) behavior in full range of strain; (**b**) enlargement of initial range of strain.

Some portion of the loading is carried out by the composite overlays through the adhesive joint.

In the obtained curve (Figure 14) a few interesting points can be observed. Till point 1, the curve is linear. The stress in point 1 corresponds to the plasticizing of the metal sample no. 3 in areas with stress concentrations. Point 1 corresponds to the strain in which the theoretical value of the maximal stress in the notch is equal to the Yield limit of the material. This stress was calculated as follows:

$$\sigma_{notch,MAX}^{theor} = \frac{Y_{eH}}{K_t} = \frac{372}{2.479} = 150 \text{ MPa}. \quad (3)$$

It can be observed that below this value the relationship between stress and strain is linear. The significant increase in the curvature of the σ-ε curve is visible for stresses above 400 MPa. This effect is clearly visible in Figure 15, where stress–strain curves for samples with square holes with a fillet radius R2 and with reinforcement (no. 5) and without composite overlays (no. 3) are compared. It should be noted that the Yield limit in sample no. 3 without reinforcement was achieved at ε_{TOT} = 0.32% (see Figure 15; it is corresponding to point 2 in Figure 14). The strain field on the composite overlays for such a loading level is visible in Figure 16c and can be compared with Figure 11a for the similar total strain for the sample without reinforcements.

In the first part of the stress–strain curve (Figure 15 for $\varepsilon_{TOT} < 0.6\%$), which is the subject of the presented analysis, the benefits of the application of composite reinforcements are visible. The first differences in stress–strain curves can be observed for stresses greater than 325 MPa. The application of the overlays significantly reduces plastic stresses in a metal part. However, it is visible that above 350 MPa the plastic deformations occur in the metal part also in sample no. 5 with overlays. In the presented example, the influence of the composite overlays on the sample behavior begins to be visible, when plasticization of the metal part exceeds some critical level (above stress 300 MPa). The sudden drop of the stress and strain is observed after the separation of the particular overlays (see magnified zones in Figure 15). After failures of both overlays (caused by failure of the adhesive joint), a strong increase in the plastic strains in a metal part is observed in the σ–ε curve. This means that above 400 MPa, the overlays carry the greater part of the growing tension. The total plastic deformation of the metal part can be observed after the separation of both

overlays (for strain ε_{TOT} = 0.65%). Both failures of reinforcement overlays are caused by the exceeding of shear stresses in adhesive joints.

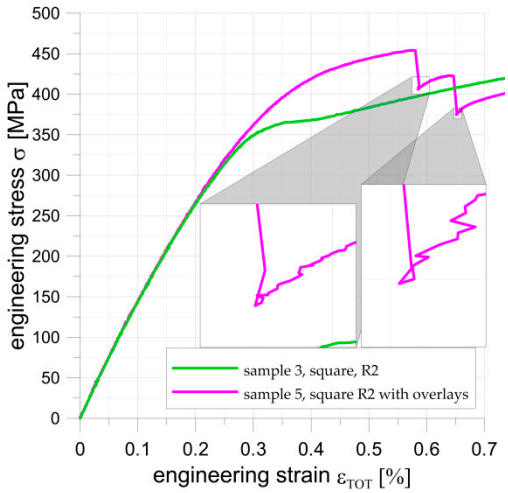

Figure 15. Comparison of engineering stress–strain curve metal sample 3 and sample 5 with composite overlays with square holes with fillet radii R2.

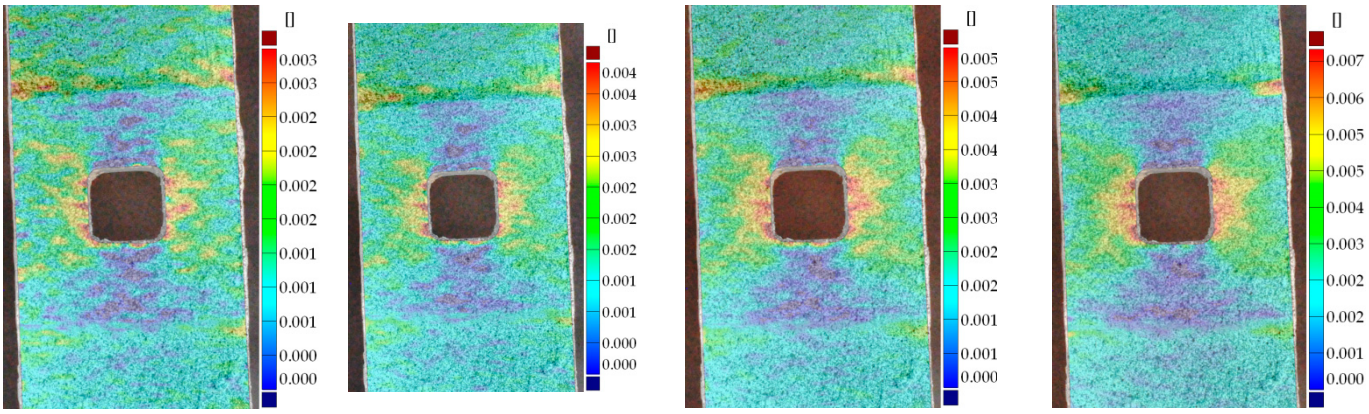

Figure 16. Distribution of strain on surface for sample no. 5 with rectangular holes with a fillet radius of R2 and composite overlays for strain: (**a**) ε_{TOT} = 0.22%; (**b**) ε_{TOT} = 0.27%; (**c**) ε_{TOT} = 0.32%; (**d**) ε_{TOT} = 0.37%.

The first cracks in the adhesive joint are observed in the photographs for total strain ε_{TOT} = 0.5% (point 3 in Figure 14). This can be also observed in the results from DIC in Figures 17 and 18. The maximal stress for the sample with overlays is equal to 453 MPa (p. 4 in Figure 14). For such loading conditions, the first overlays are separated from the metal part. After the failure of the first overlay, the stress is reduced to 406 MPa. The second overlay is separated for stress equal to 422 MPa, and after that, the whole loading is carried only by the metal part.

A significant role in the failure of the sample with composite reinforcements plays stress concentrations. In this case, the high strain concentrations occurred in:

1. The metal part—four points (not visible in presented attached Figures, but can be assessed in the example of the plate without reinforcements—Figure 11);
2. The composite overlays/adhesive joint—three points on each vertical edge of the rectangular hole; two points in the rounded corner and one in the middle length of the hole (Figure 16; Figure 17);
3. The adhesive joint—four points at the corners of the reinforcement overlays (Figures 16–18).

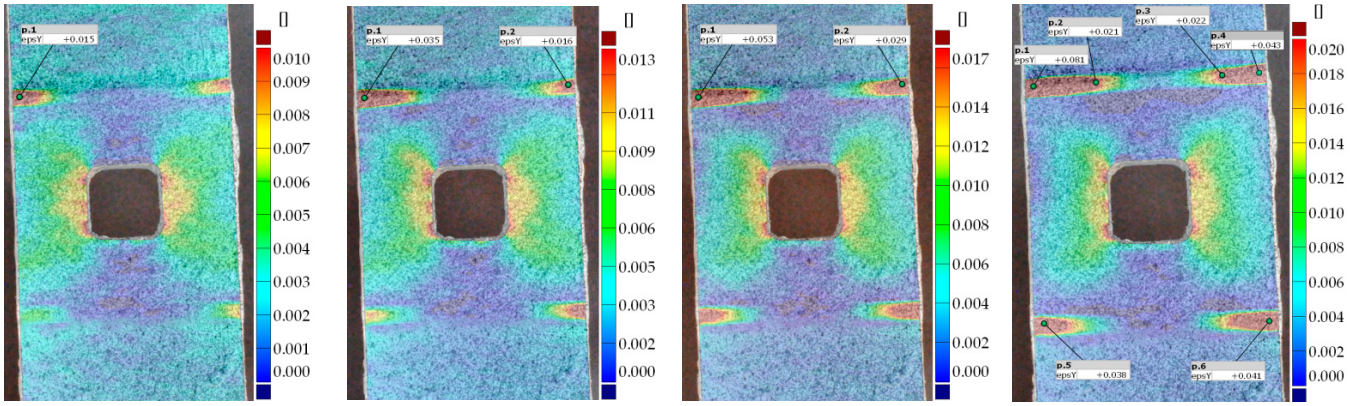

Figure 17. Distribution of strain on surface for sample no. 5 with rectangular holes with a fillet radius R2 and composite overlays for strain: (**a**) ε_{TOT} = 0.42%; (**b**) ε_{TOT} = 0.48%; (**c**) ε_{TOT} = 0.52%; (**d**) ε_{TOT} = 0.57%.

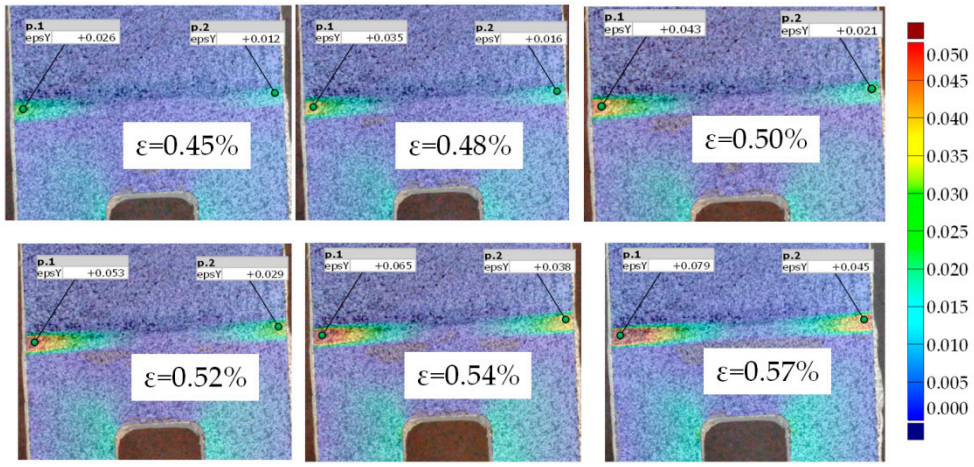

Figure 18. Development of strains and damage in adhesive joints for different ε_{TOT}.

Due to the fact that the concentrations in the metal part are not determined in the DIC analyses, the further comparison is limited to the strains in composite overlays and strains achieved in adhesive joints. For the lower tensile load (total strain ε_{TOT} < 0.4%—Figure 16), the higher strains occurred in the composite overlays around the rectangular hole. For higher strains, the strain concentrations are the highest in the adhesive joints (Figure 17). Such concentrations grow from each end of rectangular reinforcement and the increase of these strains is significantly greater than the increase in the strains around the rectangular hole. This is probably caused by the decrease in the stiffness of the metal part (due to the plasticization in the range of the yield plateau and strain hardening) placed between the overlays. This leads to the situation in which the stiffness of the composite overlays is higher than the stiffness of the metal part. The further growth of the external load is redistributed between the steel panel and composite overlays and this redistribution depends on the tension stiffness of the respective parts. The straight assessment of this phenomenon is difficult to evaluate due to the spread of the plastic, weakened zone in steel plate, the size of which strongly influences the final tension stiffness of the steel part. It should be also noted that in this case, the adhesive joint is the weakest part of the sample.

On the basis of the taken photographs and the performed DIC analysis, it is difficult to determine what part of the overlay carried the load. However, it seems that both ends of the overlays (5 mm length from upper and bottom overlay end—see Figure 17 and areas on the overlays with dark blue color) are much less loaded. This is probably caused by the described-above effect of the reduction in the stiffness of the metal part. Let us compare

distributions of strains in two samples: with composite overlays (Figure 17) and sample 3 without overlays (Figure 11). It can be seen that the area in which strains occurred on the overlay surface is similar to the area in which large plastic deformation occurs in the plate without overlays (Figure 19). The final failure form of sample no. 5 with composite overlays is given in Figure 20.

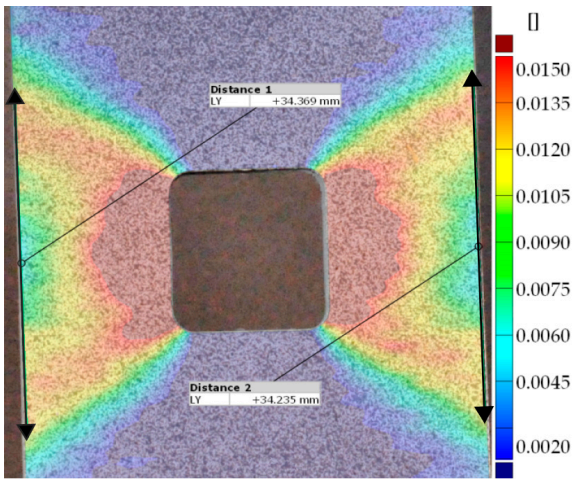

Figure 19. Distribution of strains for sample 3 (without overlays) for ε_{TOT} = 0.48%.

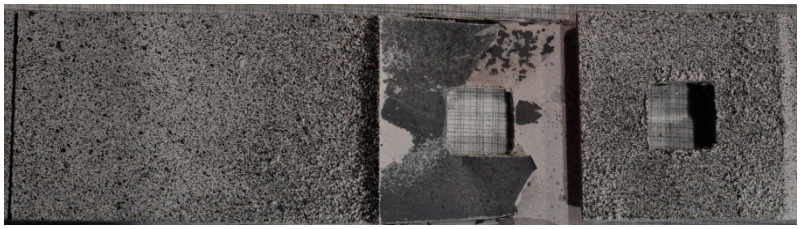

Figure 20. Final failure of sample 5.

4. Finite Element Analyses

The lack of the respective analytical solutions in the studied cases can be compensated by the numerical analysis. For that purpose, the finite element approach has been involved, and the ANSYS software [61] was used. The respective numerical analysis can be performed on various levels of approximation, in the general case the structure can be regarded as the 3D object, which demands the application of 3D solid finite elements. The main drawback of such an approach is the size of the numerical task, which should be solved to get reliable results. The reason for this is the need for the application of very dense mesh in the vicinity of notches to precisely predict and illustrate the stress concentration effect. The compromise in this is the application of the 2D shell or plane models, which are fully justified due to the small, in comparison with the remaining dimensions, thickness of the analyzed plate. In general, the ANSYS software offers different types of finite elements, which can be used for the analysis of orthotropic, layered laminates or their combinations with isotropic materials. Among them, there are the two finite strain shell elements, two layered structural solid elements and 3D layered structural shell elements, which allows for the inclusion of laminates with even 250 independently defined layers. The essential difference between the above-mentioned elements relies on the approximation level of the searched displacements. These can be modeled by polynomials with linear or quadratic shape functions. Here, in this paper, the finite strain shell elements with linear approximation (SHELL181) were used for the calculations. The main reason for this was because the thickness of the analyzed structure was several times smaller than the remaining dimension of the plate ($W/t > 10$). The detailed numerical calculations were

performed for the formerly investigated experimentally flat samples with the circular hole or the rectangular hole with rounded corners with a fillet radius R2. The obtained results were compared between the plates without overlays and with overlays. The three types of overlays are of common use. These were: overlays in the shape of the circular patch, overlays of the rectangular shape and overlays in the form of two thin stripes located by the side of the cut hole directed along the tension direction. The first two shapes seem more justified for structures with local voids, like holes, while the last one is more suitable for long slabs with cracks or elements with external undercuts. The finite element meshes used in the calculations exhibited the common feature, which was as follows—the use of the relatively dense meshes with small elements around the notches and in their neighborhood. This allows obtaining a precise approximation of the strain and stress values, in the notches and their nearby zones and the application of rather moderate meshes in the areas, which are not the main interest. The quality of the applied approximation is controlled by the *h*-convergence study in notches, observation of regularity of the strain or stress contours, and the control of the agreement of the results in symmetrically located points, with respect to the vertical middle cross-section of the samples. This is valid, of course, for cases with no composite overlays or for samples with overlays with fiber orientation $\theta = 0^\circ$ or 90° with respect to the tension direction. The exemplary mesh for the plate with the rectangular hole with rounded corners is presented in Figure 21. The analogous meshes were used for the remaining notches.

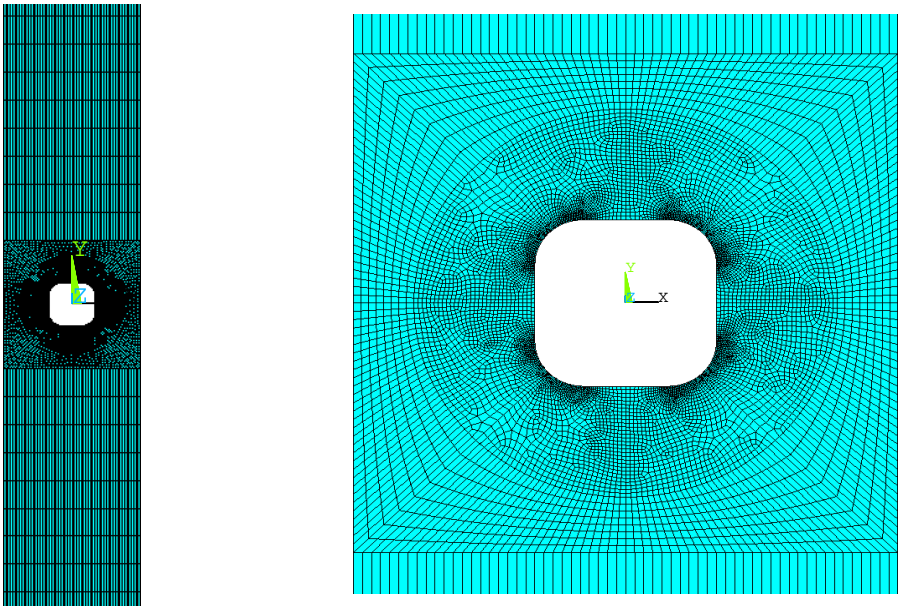

(**a**) (**b**)

Figure 21. Finite element mesh: (**a**) general view; (**b**) enlargement of the notch and circular overlay area.

The detailed numerical calculations were performed for the stacking sequence as follows (see Figure 3b): the layer with the number 9 corresponds to the steel plate, while the layers from 1 to 8, and 10 to 17 are the fiber-reinforced composite layers, with the respective angle orientation. The FE analysis was performed for the flat bar with the length of 200 mm, the width of 45 mm and the thickness of 4 mm (Figure 2). In such a flat element the respective rectangular or circular holes were made. The sizes of the openings were chosen in such a way that the nominal stress in the weakened cross-section was equal to 8.33 MPa, which meant that the diameter of the circular hole was set to 15 mm and for the rectangular void, the distance between the opposite straight sides was assumed to be the same. The samples were subjected to the tension force F = 1000 N in the vertical direction at

the bottom, while the upper edge was fully clamped. Such a configuration fully followed the experimental tests. In the first step, the samples with no overlays were analyzed to get the basis for the stress concentration comparisons. Figure 22 illustrates the numerically obtained stress concentrations observed in the weakened hole sample cross-section.

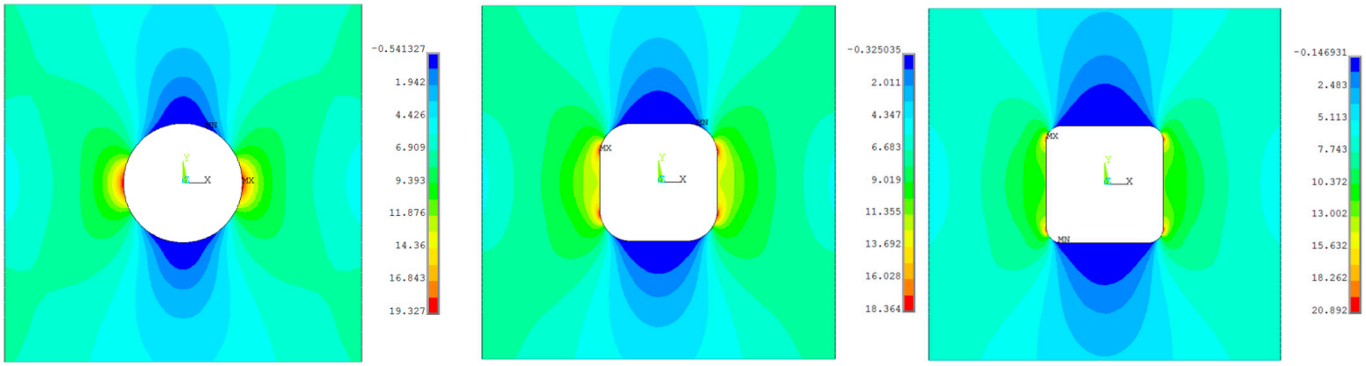

(**a**) (**b**) (**c**)

Figure 22. Distribution of σ_y stress for three analyzed samples without reinforcements: (**a**) circular hole—sample 2; (**b**) rectangular hole with fillet radius R4—sample 3; (**c**) rectangular hole with fillet radius R2—sample 4.

The above results are considered the reference solutions taken for comparison in further assessment of the applied overlay effectiveness. Due to the fact that numerous investigations have been made for plates with circular holes, the presented study is concentrated on the experimental and numerical investigations for the samples with rectangular holes.

4.1. Circular Patch

In Figures 23–25, the stress distributions in the analyzed samples with composite overlays are presented. This set concerns the results obtained for the circular patch placed around the rectangular hole. In Figure 23, the distribution of tension stress is presented for the radius of the overlay set to R_{ov} = 20 mm and for the fiber orientation θ = 0°. Such a combination provided the minimum stress concentration for the studied sample and overlay configurations. In Figure 24 the comparison of the tension stresses is shown for different fiber orientation angles and for R_{ov} = 20 mm. These stresses are shown in the area just below the circular patch. In Figure 25 the respective tension stresses in the top layer of the overlay are shown.

Due to the fact that the points with the maximum value of the tension stress occupy different positions around the circumference of the void (these points are always located in the notch area), the plots are constructed in such a manner that point C always corresponds to the point with the maximum stress value, but point D is the point located on the outer edge of the sample with the vertical coordinate equal to the 'y' coordinate of point C (Figure 26). In Figure 27a the distribution of tension stress along the line CD is shown. Here the results are given for the θ = 0° fiber orientation and for different sizes of the circular patch. Such fiber orientation provides the maximal reduction of the stress concentration. In Figure 27b the results of tension stress along the CD line are presented for different fiber orientations and for the set value of the outer radius of the circular patch (R_{ov} = 17.5 mm). It is visible that the orientation of fibers along the tension direction in overlays provides the maximum stress reduction.

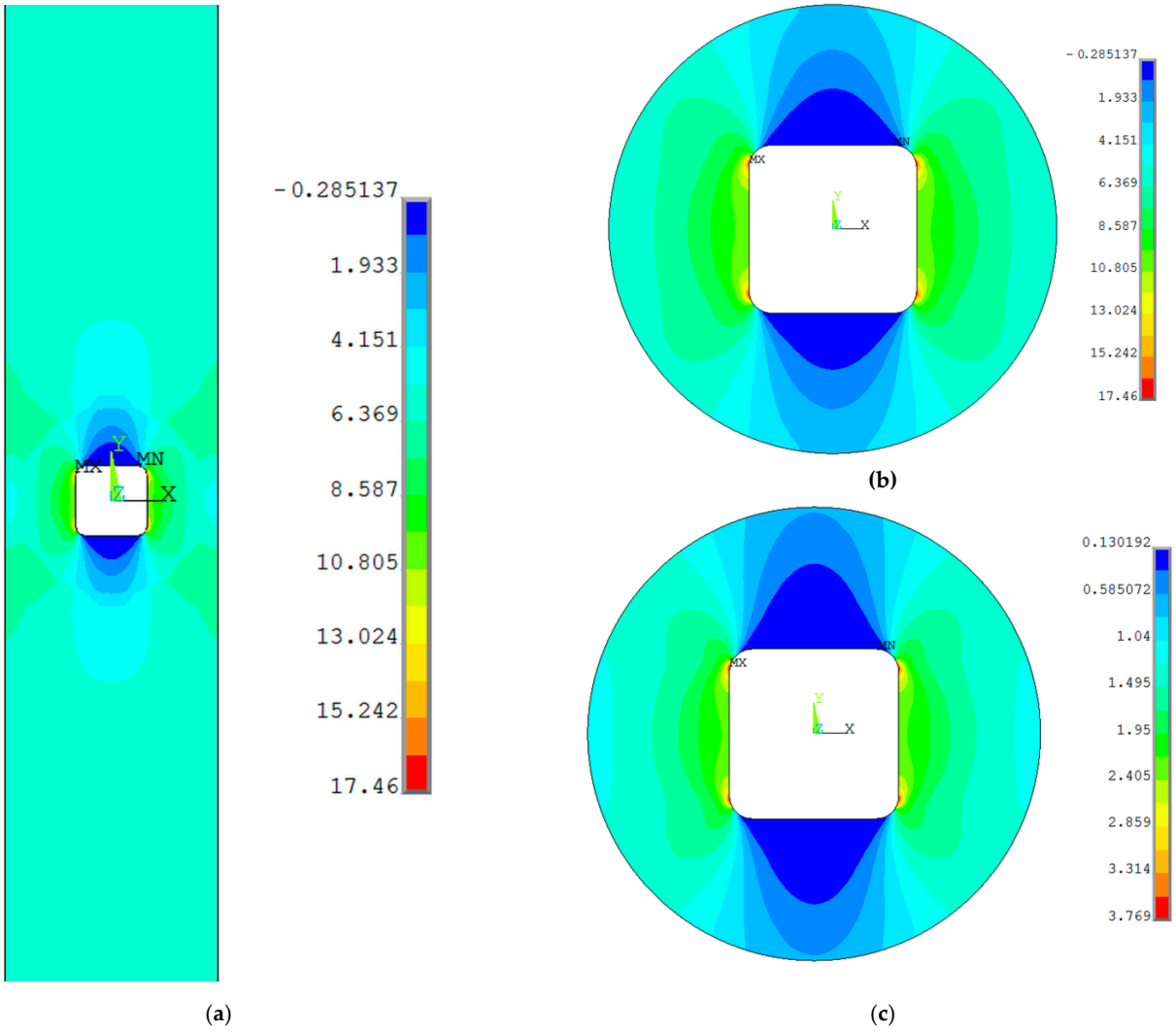

Figure 23. Distribution of tension stress σ_y in steel panel for circular patch overlay with R_{ov} = 20.0 mm and θ = 0°: (**a**) in the whole sample; (**b**) in steel part area under patch; (**c**) in composite layer.

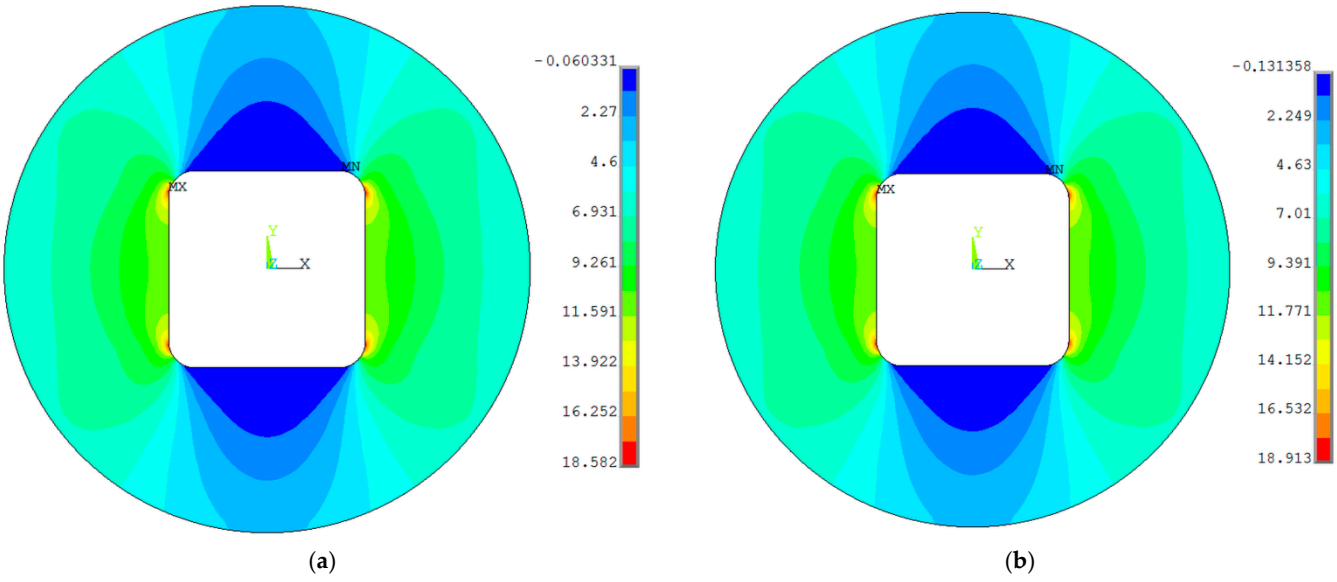

Figure 24. *Cont.*

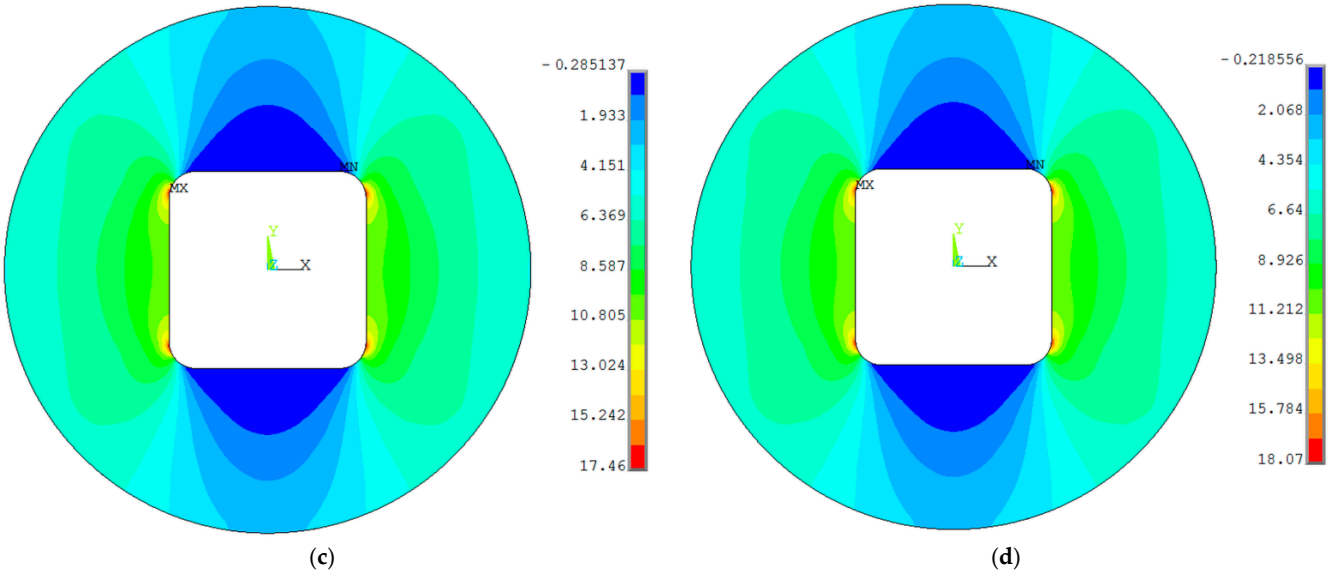

(**c**) (**d**)

Figure 24. Distribution of tension stress σ_y for circular patch in with R_{ov} = 20 mm steel part under circular patch: for different fibre angle orientation: (**a**) θ = ±45°; (**b**) θ = 90°; (**c**) θ = 0°; (**d**) θ = 0°/90°.

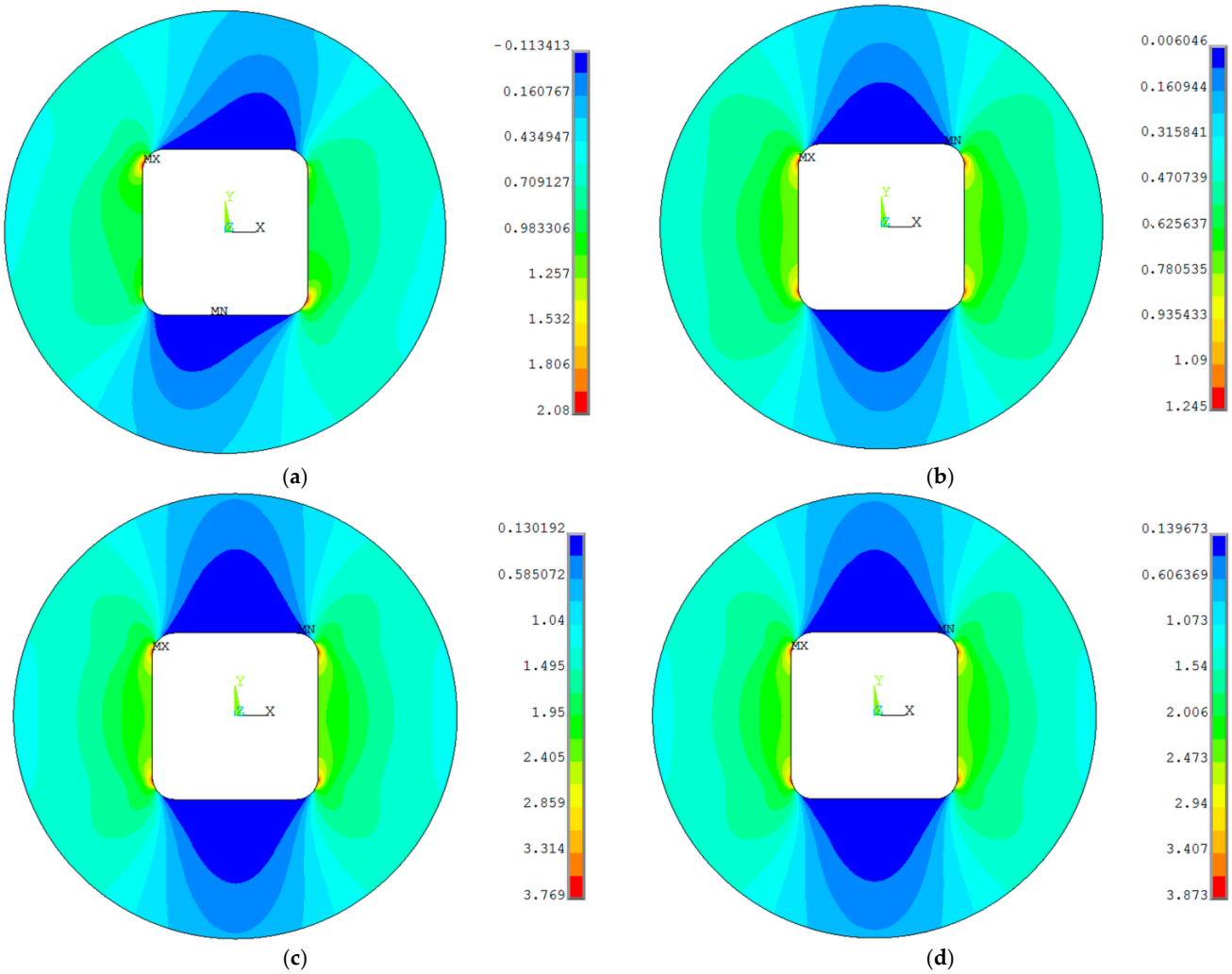

(**a**) (**b**)

(**c**) (**d**)

Figure 25. Distribution of tension stress σ_y^{comp} for top composite layer, patch size: R_{ov} = 20 mm, for different fiber angle orientation: (**a**) θ = ±45°; (**b**) θ = 90°; (**c**) θ = 0°; (**d**) θ = 0°/90°.

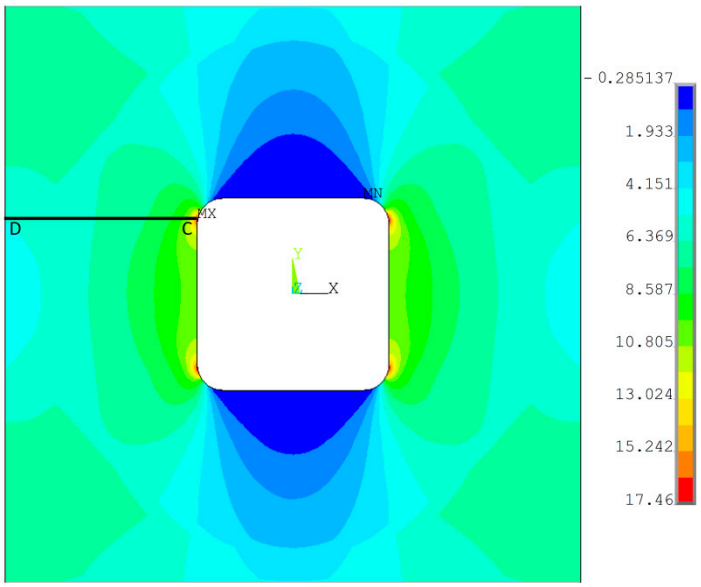

Figure 26. Path CD used for plots for distribution of tension stress σ_y.

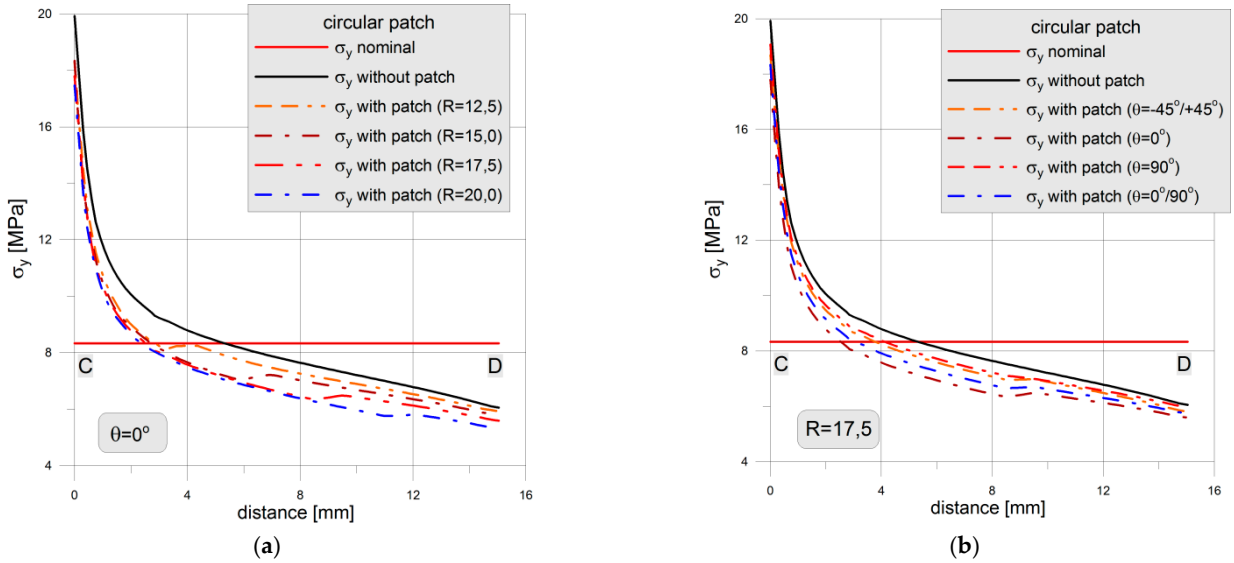

Figure 27. Distribution of tension stress σ_y for different size of circular overlay for θ=0°: (**a**) for different values of patch outer radius; (**b**) for different angle of fiber orientation.

4.2. Square Patch

Figure 28 is not to scale drawing of the mesh of finite elements for the square patch, while in Figures 29–31, the stress distributions in analyzed samples with composite overlays are presented. This set concerns the results obtained for the square patch placed around the rectangular hole. The distribution of tensile stress in the steel part is presented for different fiber orientations are presented in Figure 29. As previously, the θ = 0° fiber orientation provides the maximum stress reduction. In Figure 30 the respective distributions of vertical stresses on the outer composite layer are presented. Figure 31 shows the distribution of the vertical stresses in the most strenuous weakened cross-section of the steel panel.

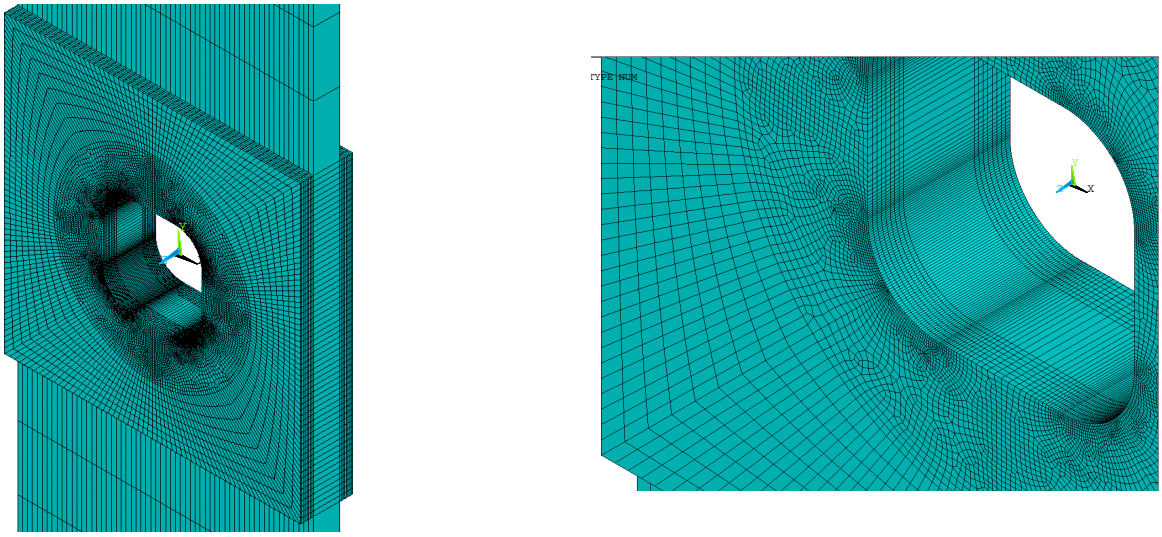

(**a**) (**b**)

Figure 28. Mesh of finite elements for sample with full width rectangular overlay, real thickness of respective layers shown in magnification: (**a**) overlay area perspective view; (**b**) detail of corner area.

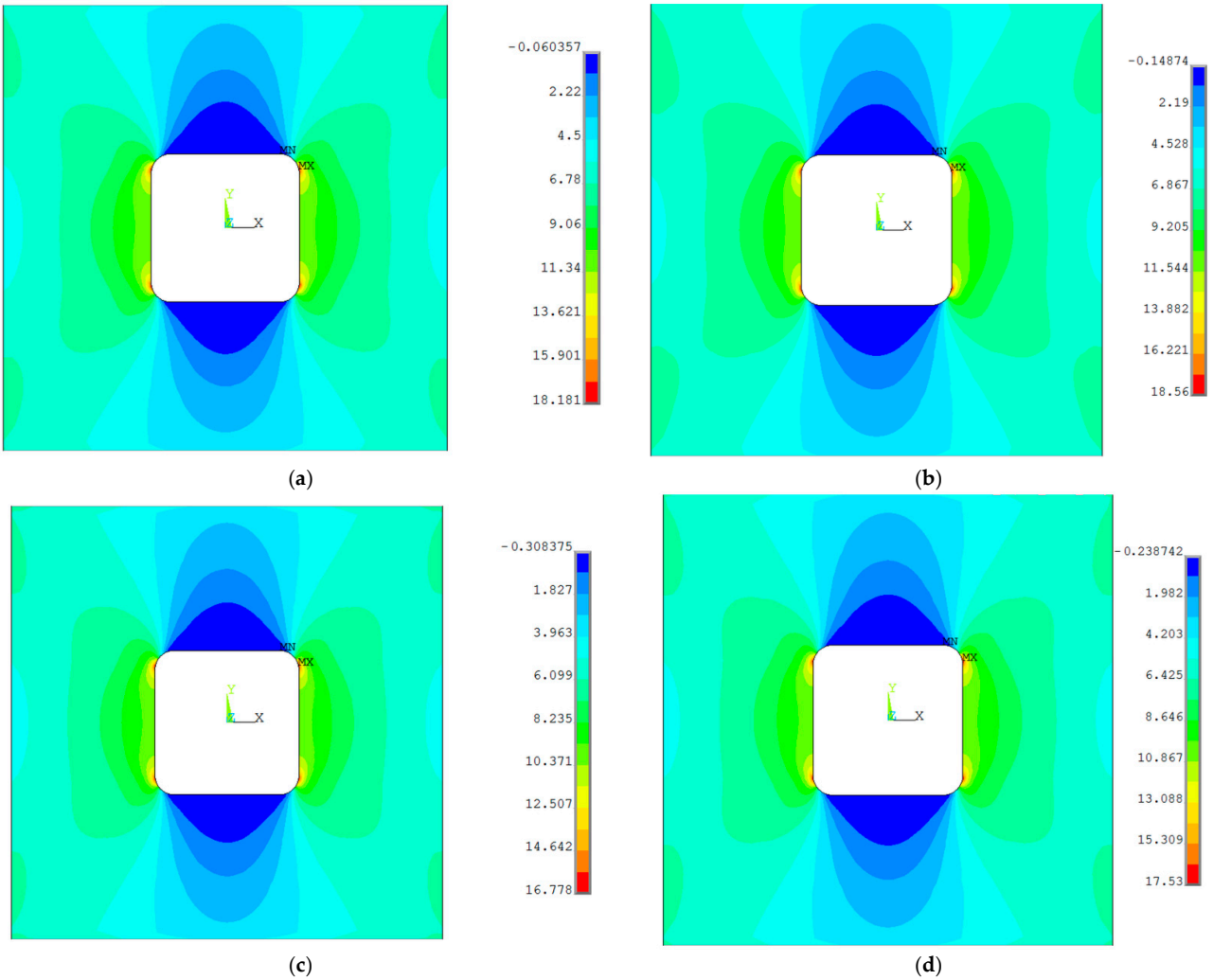

(**a**) (**b**)

(**c**) (**d**)

Figure 29. Distribution of tension stress σ_y for square patch in steel part (45 × 45) under patch: for different fiber angle orientation: (**a**) θ = ±45°; (**b**) θ = 90°; (**c**) θ = 0°; (**d**) θ = 0°/90°.

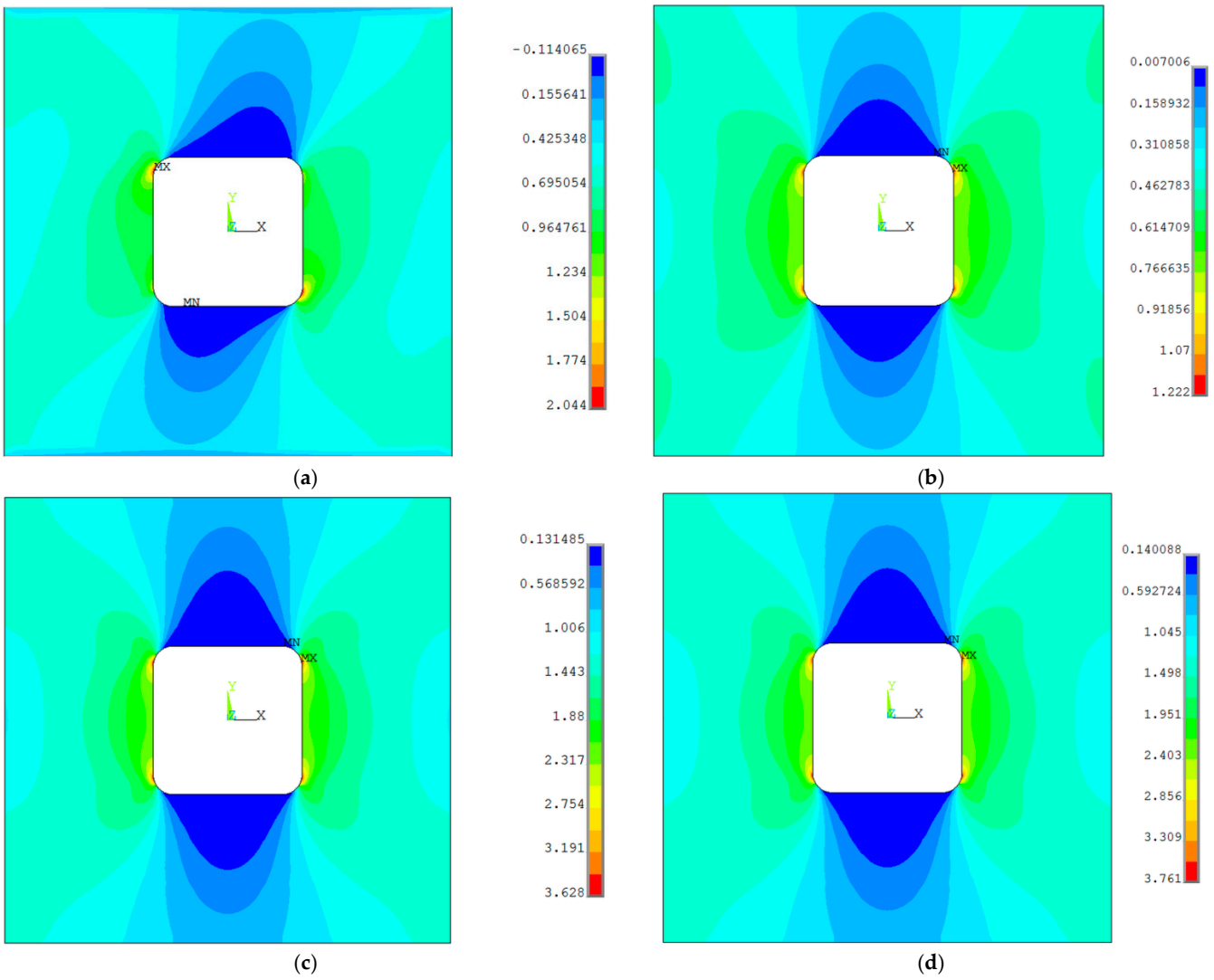

Figure 30. Distribution of tension stress σ_y^{comp} for top composite layer for square patch (45 × 45), for different fiber angle orientation: (**a**) θ = ±45°; (**b**) θ = 90°; (**c**) θ = 0°; (**d**) θ = 0°/90°.

A summary of the obtained numerical results is given in Table 5. The analysis of them says that the bigger size of the overlay gives the lower stress concentration in the notch area in order that the maximum stress reduction is obtained for the square patch, which covers the full width of the sample. Additionally, the most convenient stacking sequence is the one with fibers placed parallel to the tension load direction. This conclusion is obvious for the analyzed set of loadings, but fails in the general case, where the system of external loads becomes more complex. In such a situation the best orientation of fibers should be set in the optimization process. The tension stresses in the vertical direction obtained for the outer composite layer are rather low. This observation joined with a rather moderate reduction of the maximum stress in a steel notched part, means that the applied overlay are too stiff and their tension stiffness should be reduced. This observation opens an area for the search of optimal—in a view of stress reduction—choice of the overlays, including material of fibers, number of applied layers, fiber orientation, and stacking sequence, which in sum define the overlay stiffness.

In this set of analyzed problems, it is worth mentioning that the maximum values for the tension stress in the notch appearing in the steel part are observed in the different rounded corners, but the maximum values for the remaining three notches remain almost the same within the calculation error (the software shows the maximum sign only for one point, even if the values in the three remaining points are the same).

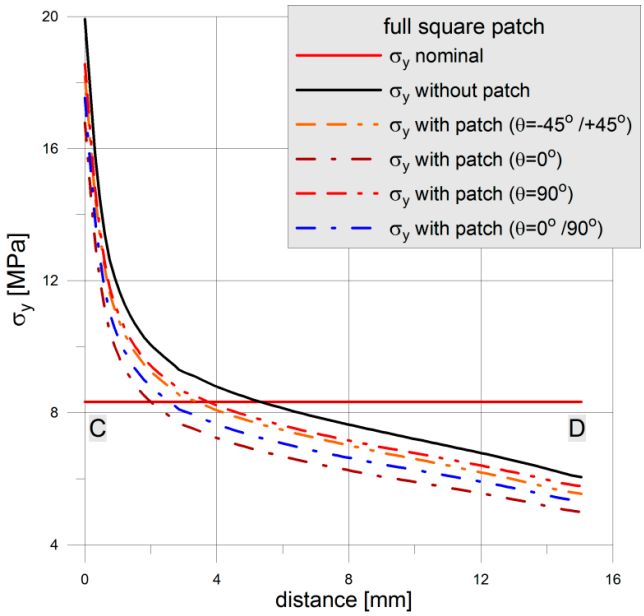

Figure 31. Square patch 45 × 45, distribution of tension stress σ_y: for different angle of fiber orientation.

Table 5. Numerical results, Hexcel TVR380, width W = 45 mm, plate thickness t = 4 mm, σ_{nom} = 8.33 MPa, square hole with fillet radius R2, two overlays with 8 layers each, θ—fiber angle orientation in layers with respect to tension direction.

Overlay Data In (mm)	K_t (−)	$\sigma_y^{comp}/\sigma_{nom}$ [1]	θ
No Overlay			
-	2.508	0.301	-
Circular Patch			
R_{ov} = 12.5	2.262	0.262	$[-45°/45°]_4$
R_{ov} = 15.0	2.289	0.260	$[-45°/45°]_4$
R_{ov} = 17.5	2.242	0.253	$[-45°/45°]_4$
R_{ov} = 20.0	2.231	0.250	$[-45°/45°]_4$
R_{ov} = 12.5	2.195	0.357	$[0°]_8$
R_{ov} = 15.0	2.201	0.359	$[0°]_8$
R_{ov} = 17.5	2.135	0.342	$[0°]_8$
R_{ov} = 20.0	2.096	0.452	$[0°]_8$
R_{ov} = 12.5	2.305	0.152	$[90°]_8$
R_{ov} = 15.0	2.334	0.154	$[90°]_8$
R_{ov} = 17.5	2.288	0.151	$[90°]_8$
R_{ov} = 20.0	2.270	0.149	$[90°]_8$
R_{ov} = 12.5	2.243	0.484	$[90°/0°]_4$
R_{ov} = 15.0	2.258	0.488	$[90°/0°]_4$
R_{ov} = 17.5	2.200	0.473	$[90°/0°]_4$
R_{ov} = 20.0	2.169	0.465	$[90°/0°]_4$
Rectangular Patch			
Size (45 × 45)	2.183	2.044	$[-45°/45°]_4$
Size (45 × 45)	2.014	3.628	$[0°]_8$
Size (45 × 45)	2.228	1.222	$[90°]_8$
Size (45 × 45)	2.104	3.761	$[90°/0°]_4$

[1] The values of vertical stress in outer composite layer σ_y^{comp} are related to the nominal stress in metal part.

5. Discussion

The main aim of this study was to attempt to increase the strength of structures with cut-outs. In the presented preliminary studies, this has been done through the application of the composite overlays on both sides of the metal sample with the cut-

out. Such reinforcement by the composite overlays is investigated in the paper in the example of the sample with the square hole with a fillet radius R2. The influence of the composite reinforcement on the sample strength is presented in Figure 32. All the figures present nominal stresses in weakened cross-sections in the metal part. It can be seen that the strength of the sample with reinforcements is higher than the strength of the other tested samples 2–4 with circular and square holes. It should also be noted that the experimentally tested sample no. 5 with composite reinforcements has the cut-out with the largest stress concentration factor K_t = 2.479 (Table 4) in comparison with other cut-outs (circular hole—K_t = 2.314 and square with filler radius R4–K_t = 2.084). Despite, the highest K_t, the composite reinforcements significantly increased the strength of the structure in comparison with samples with smaller stress concentrations (Figure 32).

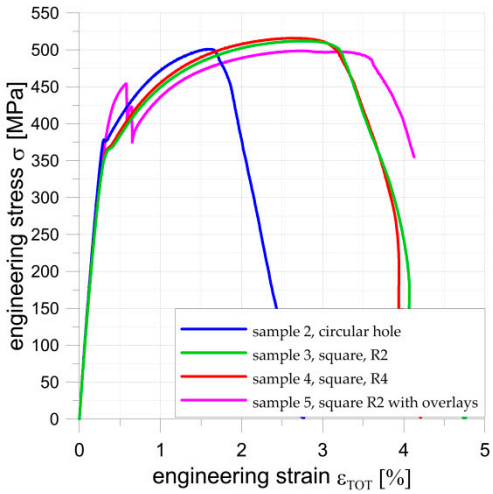

Figure 32. Comparison of engineering stress–strain curve for samples 2–4 with different cut-outs and sample 5 with a square hole with composite overlays.

Comparing the obtained results to the Yield limit of sample no. 3, the maximal stress is increased from 365 MPa (sample no. 3 without reinforcement) to 454 MPa (sample with composite reinforcements). This difference of $\Delta\sigma$ = 89 MPa means that the load-carrying capacity of the sample with reinforcements is increased by almost 25% before the damage of the overlays.

Taking into account the maximal tensile force at the moment of the failure of the adhesive joint, the minimal average shear stress in the adhesive joint is equal to:

$$\tau_{avg} = \frac{F_{max}}{A_{adh}} = 5.9 \text{ MPa}. \quad (4)$$

This value is significantly lower than the minimum shear strength of the adhesive joint, but it should be noted that in the adhesive joint there are large stress concentrations. Such stress concentrations are around the hole and at the ends of the adhesive joints. The value of the stress concentrations at the end of the bounded joint often achieves high values [40,41,45,51]. This value depends on the stiffness of the adherents, the adhesive shear modulus and thickness, and the geometry of the joint (overlap width and length). The distribution of the shear stresses is calculated using FEM. It allows determination of the stress concentrations around the hole. However, the determination of the stress concentrations at the ends of the adhesive is impossible with the use of the applied numerical model. This problem requires further analyses with the application of the 3D FEM analyses.

The results are presented for the maximal tensile loading (ε_{TOT} = 0.57%) just before separation of the first overlay (p. 4 in Figure 14). In Figure 33a the distribution of the vertical strain on the external composite layer is presented. Good agreement of DIC (Figure 17d) and FEM (Figure 33a) analyses is achieved. The shear stress in the adhesive is presented

in Figure 33b. High concentrations of stresses can be observed in the surroundings of the notches of the rectangular hole in both composite overlays (Figure 33a) and in adhesive epoxy (Figure 33b). The value of shear stresses around the notch significantly exceeds the admissible value of 27 MPa. This justifies further optimization of the adhesive joint consisting in determining the optimal design of the adhesive joint (overlay shape and size, orientation of the layers, adhesive type and thickness, and shape of the hole).

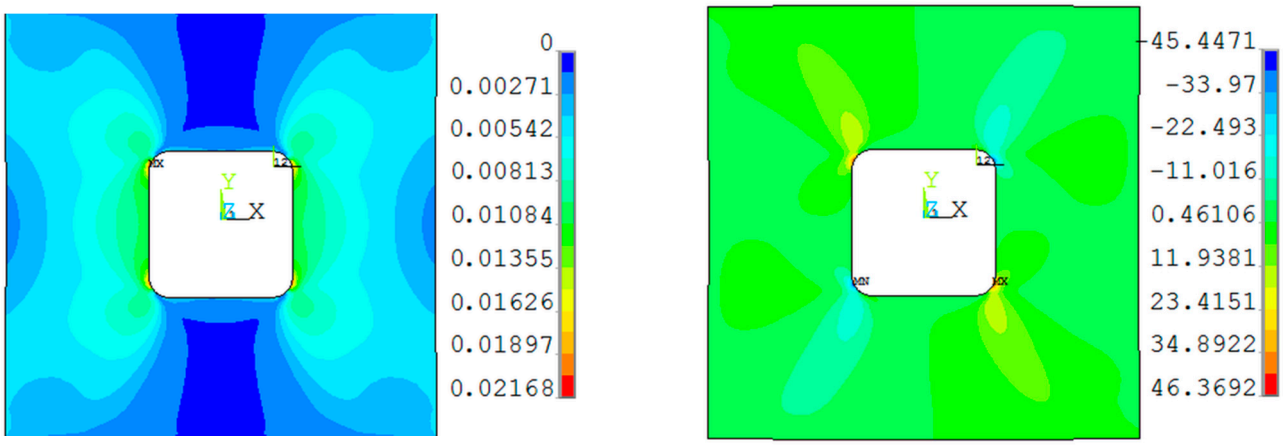

(**a**) (**b**)

Figure 33. FE results for sample 5 with composite overlays, ε_{TOT} = 0.57%: (**a**) vertical stress σ_y in layer no. 19 (external surface); (**b**) shear stress in adhesive layer.

The two typical shapes of the composite overlays were studied and the influence of size, shape and different fiber orientations were numerically investigated. The finite element mesh was chosen in such a way that the highest density of the elements was introduced in the area neighboring notches. The generated element meshes over the whole sample mimics the symmetry of the structure. However, due to the application of the composite layers and their fiber orientations, the symmetry conditions were not used for all analyzed cases. The obtained result show the reduction of stress concentrations in the hole corners after application of the overlays. The most convenient fiber orientation for both studied corner radii is that one, in which the fibers were set along the direction of the applied external tension load ($\theta = 0^\circ$). In the remaining fiber orientations, the influence of the overlays on the stress reduction was smaller. It appeared that the bigger the size of the overlay, the higher the reduction of the maximum stress is observed. In this context, the square overlay appeared to be the most effective, giving 20% of the maximum stress reduction for fiber orientation $\theta = 0^\circ$. However one must be aware that in the practical application, the size of the overlay may be limited by different factors, such as the general size of the object, etc. The summary of the effectiveness of the studied overlays can be expressed in the percentage reduction of the stress concentration factor in the steel plate part (see Table 6).

Table 6. Reduction of stress concentration K_t in (%).

Patch Type	Overlay Fiber Orientation θ with Respect to Tension Direction			
	$[-45^\circ/45^\circ]_4$	$[0^\circ]_8$	$[90^\circ]_8$	$[90^\circ/0^\circ]_4$
Circular, R_{ov} = 20, R2	10.7	15.7	9.5	13.5
Square 45 × 45, R2	13.5	20.4	11.1	16.1

If the composite overlays are to be applied, then the proper choice of overlays data becomes more complex and must include the influence of the number of layers, the stacking sequence of them and the size of the overlay. The numerical analyses performed in the

paper relied on the use of layered shell elements. In such an analysis, it is difficult to model and study the influence of the applied bonding layer (glue layer). In the further analysis, it is planned to perform full 3D analysis with the inclusion of the mechanical properties of the applied bonding layer. Here an additional problem would concern the choice of the kind of adhesive, its thickness, and the mechanical properties. It is also planned to perform the investigations for other radii notches (for rectangular hole) and for different shapes of notches used in practice.

6. Conclusions

The performed experimental and numerical study let us draw the following conclusions:

- the good agreement between the DIC results with the FEM results has confirmed the usefulness of the DIC tool and GOM software in the non-destructive analysis of structural elements;
- the effectiveness of the composite overlay application has been confirmed by the reduction of the stress concentration factor in the notch area. In the investigated example, the application of the square composite overlay increased the structure strength even by 25%;
- the stress concentration reduction is the function of the fiber orientation and is the highest in the case of fibers set in parallel to the applied loading;
- the bigger size of the overlay patch the bigger reduction of the stress concentration is observed.

Author Contributions: Conceptualization, P.J.R., B.S. and M.W.; investigation, P.J.R., B.S. and M.W.; data curation, P.J.R., B.S. and M.W.; writing—original draft preparation, P.J.R., B.S. and M.W.; writing—review and editing, P.J.R., B.S. and M.W. All authors have read and agreed to the published version of the manuscript.

Funding: This research received no external funding.

Conflicts of Interest: The authors declare no conflict of interest.

References

1. Romanowicz, P.J.; Szybiński, B.; Wygoda, M. Application of DIC Method in the Analysis of Stress Concentration and Plastic Zone Development Problems. *Materials* **2020**, *13*, 3460. [CrossRef] [PubMed]
2. Huang, B.T.; Li, Q.H.; Xu, S.L.; Li, C.F. Development of reinforced ultra-high toughness cementitious composite permanent formwork: Experimental study and Digital Image Correlation analysis. *Compos. Struct.* **2017**, *180*, 892–903. [CrossRef]
3. Muc, A.; Chwał, M.; Romanowicz, P.; Stawiarski, A. Fatigue-Damage Evolution of Notched Composite Multilayered Structures under Tensile Loads. *J. Compos. Sci.* **2018**, *2*, 27. [CrossRef]
4. Muc, A.; Romanowicz, P. Effect of notch on static and fatigue performance of multilayered composite structures under tensile loads. *Compos. Struct.* **2017**, *178*, 27–36. [CrossRef]
5. Kirsch, E.G. Die Theorie der Elastizität und die Bedürfnisse der Festigkeitslehre. *Z. Ver. Dtsch. Ing.* **1898**, *42*, 797–807.
6. Kolosov, G.V. *Application of Complex Diagrams and the Theory of Functions of a Complex Variable to the Theory of Elasticity*; ONTI: Moscow, Russia; Leningrad, Russia, 1935; 224p. (In Russian)
7. Inglis, C.E. Stress in a plane due to the presence of cracks and sharp corners. *Trans. Inst. Naval. Archit.* **1913**, *55*, 219–241.
8. Neuber, H. *Kerbspannungslehre: Grundlagen für genaue Festigkeitsberechnung mit Berücksichtigung von Konstruktionsform und Werkstoff*, 4th ed.; Springer: Berlin, Germany, 2001. [CrossRef]
9. Savin, G.N. Savin, G.N. *Stress Distribution around Holes (Translated from Russian) NASA Technical Translation NASA TT F-607*; NASA: Washington, DC, USA, 1970; 300p. Available online: https://archive.org/details/nasa_techdoc_19710000647/page/n1/mode/2up (accessed on 18 May 2021).
10. Mushkelishvilli, N. *Some Basic Problems of the Mathematical Theory of Elasticity*; Springer: Dordrecht, The Netherlands, 1977.
11. Howland, R.C.J. On the stresses in the neighborhood of a circular hole in a strip under tension. *Philos. Trans. R. Soc. (Lond.) Ser. A* **1930**, *229*, 49–86.
12. Lekhnitskii, S.G. *Theory of Elasticity of an Anisotropic Body*; Mir Publishers: Moscow, Russia, 1981; 431p. (In Russian). Available online: https://www.twirpx.com/file/762362 (accessed on 18 May 2021).
13. Tan, S.C. Finite-width correction factors for anisotropic plate containing a central opening. *J. Compos. Mater.* **1988**, *22*, 1080–1097. [CrossRef]
14. Rezaeepazhand, J.; Jafari, M. Stress concentration in metallic plates with special shaped cutout. *Int. J. Mech. Sci.* **2010**, *52*, 96–102. [CrossRef]

15. Tanaka, K.; Nakai, Y. Prediction of fatigue threshold of notched components. *Trans. ASME* **1984**, *106*, 192–199. [CrossRef]
16. Smith, R.A.; Miller, K.J. Prediction of Fatigue Regimes in Notched Components. *Int. J. Mech. Sci.* **1978**, *20*, 201–206. [CrossRef]
17. Heywood, R.B. *Designing by Photoelasticity*; Chapman and Hall, Ltd.: London, UK, 1952.
18. Frocht, M.M. *Photoelasticity*; John Wiley & Sons: New York, NY, USA, 1957.
19. Sobey, A.J. ARC reports and memoranda No. 3407. H.M. In *Stress-Concentration Factors for Rounded Rectangular Holes in Infinite Sheets*; Stationery Office: London, UK, 1963.
20. Mitchell, M.R. Fundamentals of modern fatigue analysis for design. In *ASM Handbook, Volume 19: Fatigue and Fracture*; Lampman, S.R., Ed.; ASM International: Material Park, OH, USA, 1996; pp. 227–249.
21. Young, W.C.; Budynas, R.G. *Roark's Formulas for Stress and Strain*, 7th ed.; McGraw-Hill: New York, NY, USA, 2001.
22. Savruk, M.P.; Kazberuk, A. *Stress Concentration at Notches*; Springer International Publishing: Cham, Switzerland, 2017.
23. Pilkey, W.D.; Pilkey, D.F. *Peterson's Stress Concentration Factors*, 3rd ed.; John Wiley & Sons, Inc.: Hoboken, NJ, USA, 2008.
24. Pedersen, P. On optimal shapes in materials and structures. *Struct. Multidisc. Optim.* **2000**, *19*, 169–182. [CrossRef]
25. Szybiński, B.; Wróblewski, A. Parametric optimization of stress relief groove shape in flat ends of boilers. *J. Strain Anal. Eng. Des.* **2012**, *47*, 55–63. [CrossRef]
26. Zienkiewicz, O.C.; Taylor, R.L.; Zhu, J.Z. *The Finite Element Method: Its Basis and Fundamentals*, 6th ed.; Elsevier-Butterworth-Heinemann: Burlington, MA, USA, 2006.
27. European Committee for Standardization. *European Standard, EN 13445-3, Unfired Pressure Vessels—Part 3: Design*; European Committee for Standardization: Brussels, Belgium, 2002.
28. Angus, C.C.; Lam, J.J.; Roger, C.; Michael, C.H.Y.; Gaylene, D.K. Repair of steel structures by bonded carbon fibre reinforced polymer patching: Experimental and numerical study of carbon fibre reinforced polymer—Steel double-lap joints under tensile loading. *Can. J. Civ. Eng.* **2007**, *34*, 1542–1553. [CrossRef]
29. Łagoda, M.; Kowal, M. CFRP composite materials strengthening of flat steel elements to reduce the stresses in the steel. *Struct. Environ.* **2014**, *6*, 5–12.
30. Wang, Z.Y.; Wang, Q.Y.; Li, L.; Zhang, N. Fatigue behaviour of CFRP strengthened open-hole steel plates. *Thin-Walled Struct.* **2017**, *115*, 176–187. [CrossRef]
31. Wang, Z.Y.; Zhang, T.; Li, X.; Wang, Q.Y.; Huang, W.; Shen, M. Characterization of the effect of CFRP reinforcement on the fatigue strength of aluminium alloy plates with fastener holes. *Eng. Struct.* **2018**, *177*, 739–752. [CrossRef]
32. Wang, Y.; Zheng, Y.; Li, J.; Zhang, L.; Deng, J. Experimental study on tensile behaviour of steel plates with centre hole strengthened by CFRP plates under marine environment. *Int. J. Adhes. Adhes.* **2018**, *84*, 18–26. [CrossRef]
33. Aljabar, N.J.; Zhao, X.L.; Al-Mahaidi, R.; Ghafoori, E.; Motavalli, M.; Koay, Y.C. Experimental investigation on the CFRP strengthening efficiency of steel plates with inclined cracks under fatigue loading. *Eng. Struct.* **2018**, *172*, 877–890. [CrossRef]
34. Ye, H.; Shuai, C.; Zhang, X.; Xu, X.; Ummenhofer, T. Determination of S-N fatigue curves for damaged steel plates strengthened with prestressed CFRP plates under tension loading. *Eng. Struct.* **2018**, *175*, 669–677. [CrossRef]
35. de Medeiros, R.; Borges, E.N.; Tita, V. Experimental analyses of metal-composite bonded joints: Damage identification. *Appl. Adhes. Sci.* **2014**, *2*, 13. [CrossRef]
36. Szybiński, B.; Wygoda, M. Numerical investigations of stress concentration in reinforcement steel structure by composite overlays. *J. KONES Powertrain Transp.* **2019**, *26*, 4. [CrossRef]
37. Rudawska, A. Comparison of the adhesive joints' strength of the similar and dissimilar systems of metal alloy/polymer composite. *Appl. Adhes. Sci.* **2019**, *7*, 7. [CrossRef]
38. Tsokanas, P.; Loutas, T.; Nijhuis, P. Interfacial Fracture Toughness Assessment of a New Titanium–CFRP Adhesive Joint: An Experimental Comparative Study. *Metals* **2020**, *10*, 699. [CrossRef]
39. Derewońko, A. Failure simulation of metal-composite joints. *Fibres Text. East. Eur.* **2013**, *5*, 131–134.
40. Yahya, N.A.; Hashim, S. Stress analysis of steel/carbon composite double lap shear joints under tensile loading. *Proc. Inst. Mech. Eng. Part L J. Mater. Des. Appl.* **2016**, *230*, 88–104. [CrossRef]
41. Ghoddous, B. Theoretical Analysis of Stress Distribution in Bonded Single Strap and Stiffened Joints. *Lat. Am. J. Solids Struct.* **2017**, *14*, 256–276. [CrossRef]
42. da Silva, L.F.M.; Öchsner, A.; Adams, R.D. *Handbook of Adhesion Technology*; Springer International Publishing: New York, NY, USA, 2018; pp. 689–723.
43. Jeevi, G.; Nayak, S.K.; Kader, M.A. Review on adhesive joints and their application in hybrid structures. *J. Adhes. Sci. Technol.* **2019**, *33*, 1497–1520. [CrossRef]
44. Banea, M.D.; da Silva, L.F.M. Adhesively bonded joints in composite materials: An overview. *Proc. Inst. Mech. Eng. Part L J. Mater. Des. Appl.* **2009**, *223*, 1–18. [CrossRef]
45. Dobrzański, P.; Oleksiak, W. Design and analysis methods for composite bonded joints. *Trans. Aerosp. Res.* **2021**, *1*, 45–63. [CrossRef]
46. Volkersen, O. Die niektraftverteilung in zugbeanspruchten mit konstanten laschenquerschritten. *Luftfahrtforschung* **1938**, *15*, 41–68.
47. Goland, M.; Reissner, E. The stresses in cemented lap joints. *J. Appl. Mech.* **1944**, *66*, A17–A27. [CrossRef]
48. Stukhlyak, P.D.; Mytnyk, M.M.; Orlov, V.O. Influence of boundary interlayers on properties of composite polymeric materials (a review). *Mater. Sci.* **2001**, *37*, 80–86. [CrossRef]

49. Maruschak, P.O.; Panin, S.V.; Stachowicz, F.; Danyliuk, I.M.; Vlasov, I.V.; Bishchak, R.T. Structural levels of fatigue failure and damage estimation in 17Mn1Si steel on the basis of a multilevel approach of physical mesomechanics. *Acta Mech.* **2016**, *227*, 151–157. [CrossRef]
50. Romanowicz, P. Experimental and numerical estimation of the damage level in multilayered composite plates. *Mater. Werkst.* **2018**, *49*, 591–605. [CrossRef]
51. Carbas, R.J.C.; da Silva, L.F.M.; Madureira, M.L.; Critchlow, G.W. Modelling of Functionally Graded Adhesive Joints. *J. Adhes.* **2014**, *90*, 698–716. [CrossRef]
52. Tsai, M.Y.; Morton, J. An investigation into the stresses in double-lap adhesive joints with laminated composite adherends. *Int. J. Solids Struct.* **2010**, *47*, 3317–3325. [CrossRef]
53. Barski, M.; Kędziora, P.; Muc, A.; Romanowicz, P. Structural Health Monitoring (SHM) methods in machine design and operation. *Arch. Mech. Eng.* **2014**, *61*, 653–677. [CrossRef]
54. Salski, B.; Gwarek, W.; Korpas, P.; Reszewicz, S.; Chong, A.Y.B.; Theodorakeas, P.; Hatziioannidis, I.; Kappatos, V.; Selcuk, C.; Gan, T.H.; et al. Non-destructive testing of carbon-fibre-reinforced polymer materials with a radio-frequency inductive sensor. *Compos. Struct.* **2015**, *122*, 104–112. [CrossRef]
55. European Committee for Standardization. *EN 10025-2:2004 Hot Rolled Products of Structural Steels—Part 2: Technical Delivery Conditions for Non-Alloy Structural Steels*; European Committee for Standardization: Brussels, Belgium, 2004.
56. Romanowicz, P.; Muc, A. Estimation of Notched Composite Plates Fatigue Life Using Residual Strength Model Calibrated by Step-Wise Tests. *Materials* **2018**, *11*, 2180. [CrossRef]
57. ASTM D 3039. *Standard Test Method for Tensile Properties of Polymer Matrix Composite Materials*; ASTM International: West Conshohocken, PA, USA, 2002.
58. Ostapiuk, M.; Surowska, B. Comparative analysis of failure of Al/GFRP laminates after tensile strength test. *Compos. Theory Pract.* **2015**, *15*, 259–265.
59. European Committee for Standardization. *EN ISO 6892-1 Metallic Materials—Tensile Testing—Part. 1: Method of Test. at Room Temperature*; European Committee for Standardization: Brussels, Belgium, 2009.
60. GOM Software 2018 Hotfix 1. Available online: www.gom.com (accessed on 26 September 2018).
61. Ansys Software. Available online: www.ansys.com (accessed on 30 March 2021).